ALMA/SCUBA-2 COSMOS Survey: Properties of X-Ray- and SED-selected Active Galactic Nuclei in Bright Submillimeter Galaxies

Ryosuke Uematsu[1] , Yoshihiro Ueda[1] , David M. Alexander[2] , A. M. Swinbank[2] , Ian Smail[2] , Carolina Andonie[2] ,
Chian-Chou Chen[3] , Ugne Dudzevičiūtė[4] , Soh Ikarashi[5,6,7], Kotaro Kohno[8,9] , Yuichi Matsuda[5,10] ,
Annagrazia Puglisi[2,11] , Hideki Umehata[12,13] , and Wei-Hao Wang[14]

[1] Department of Astronomy, Kyoto University, Sakyo-ku, Kyoto, Japan
[2] Centre for Extragalactic Astronomy, Department of Physics, Durham University, South Road, Durham, DH1 3LE, UK
[3] Academia Sinica Institute of Astronomy and Astrophysics (ASIAA), No. 1, Sec. 4, Roosevelt Road, Taipei 106216, Taiwan
[4] Max-Planck-Institut für Astronomie, K'onigstuhl 17, D-69117, Heidelberg, Germany
[5] National Astronomical Observatory of Japan, Osawa 2-21-1, Mitaka, Tokyo 181-8588, Japan
[6] Junior College, Fukuoka Institute of Technology, 3-30-1 Wajiro-higashi, Higashi-ku, Fukuoka, 811-0295, Japan
[7] Department of Physics, General Studies, College of Engineering, Nihon University, 1 Nakagawara, Tokusada, Tamuramachi, Koriyama, Fukushima, 963-8642, Japan
[8] Institute of Astronomy, Graduate School of Science, The University of Tokyo, 2-21-1 Osawa, Mitaka, Tokyo 181-0015, Japan
[9] Research Center for the Early Universe, Graduate School of Science, The University of Tokyo, 7-3-1 Hongo, Bunkyo-ku, Tokyo 113-0033, Japan
[10] Graduate University for Advanced Studies (SOKENDAI), Osawa 2-21-1, Mitaka, Tokyo 181-8588, Japan
[11] School of Physics and Astronomy, University of Southampton, Highfield SO17 1BJ, UK
[12] Institute for Advanced Research, Nagoya University, Furocho, Chikusa, Nagoya 464-8602, Japan
[13] Department of Physics, Graduate School of Science, Nagoya University, Furocho, Chikusa, Nagoya 464-8602, Japan
[14] Institute of Astronomy and Astrophysics, Academia Sinica, Taipei 10617, Taiwan

Abstract

We investigate the properties of active galactic nuclei (AGNs) in the brightest submillimeter galaxies (SMGs) in the COSMOS field. We utilize the bright sample of the ALMA/SCUBA-2 COSMOS Survey (AS2COSMOS), which consists of 260 SMGs with $S_{870\,\mu m} = 0.7$–19.2 mJy at $z = 0$–6. We perform optical to millimeter spectral energy distribution (SED) modeling for the whole sample. We identify 24 AGN-host galaxies from the SEDs. Supplemented by 23 X-ray-detected AGNs (X-ray AGNs), we construct an overall sample of 40 AGN-host galaxies. The X-ray luminosity upper bounds indicate that the X-ray-undetected SED-identified AGNs are likely to be nearly Compton thick or have unusually suppressed X-ray emission. From visual classification, we identify $25^{+6}_{-5}\%$ of the SMGs without AGNs as major merger candidates. This fraction is almost consistent with the general galaxy population at $z \sim 2$, suggesting that major mergers are not necessarily required for the enhanced star formation in SMGs. We also identify $47^{+16}_{-15}\%$ of the AGN hosts as major merger candidates, which is about twice as high as that in the SMGs without AGNs. This suggests that major mergers play a key role in triggering AGN activity in bright SMGs.

1. Introduction

The supermassive black holes (SMBHs) at the centers of galaxies may play a critical role in regulating star formation within the interstellar matter (ISM) of massive galaxies (e.g., R. G. Bower et al. 2006). Previous studies have suggested a close coevolution of galaxies and SMBHs inspired by the tight bulge-mass-to-SMBH-mass correlation found in the local universe (see J. Kormendy & L. C. Ho 2013 for a review). This idea is also supported by the similarity of the cosmological evolution of star formation rate (SFR) density and the SMBH accretion rate density across $z = 0$–5 (P. Madau & M. Dickinson 2014; Y. Ueda et al. 2003, 2014). However, the main physical mechanism driving the coevolution is still unclear. Active galactic nuclei (AGNs) are key targets to solve this problem, as they are the observed manifestation of growing SMBHs (D. M. Alexander & R. C. Hickox 2012). Some

studies suggest that feedback from AGNs can affect the star formation activity of their host galaxies through outflowing material via winds and/or relativistic jets (see A. C. Fabian 2012 for a review). Therefore, studying the properties of AGNs and their host galaxies is crucial to investigate the nature of galaxy–SMBH coevolution.

Dusty star-forming galaxies (DSFGs) are an important population in this context. DSFGs are characterized by their luminous far-infrared emission from dust heated by stars, indicating their intense star formation. Theoretical studies have indicated that intense star formation activity can trigger AGN activity by injecting turbulence in the gas disks and making the gas fall into the nuclear regions (e.g., A. Hobbs et al. 2011). Some studies also suggested that starburst activity can be triggered by galaxy mergers, which subsequently trigger AGN activity (e.g., P. F. Hopkins et al. 2008; S. McAlpine et al. 2019). Hence, DSFGs may be useful targets for studying the triggering mechanism of AGNs. Sub/millimeter observations are powerful tools to detect high-redshift DSFGs. At higher redshift, the peak of dust emission is redshifted to the sub/ millimeter bands. Thus, high-redshift DSFGs are commonly referred to as submillimeter galaxies (SMGs) owing to their

selection wavelength. The Atacama Large Millimeter/submillimeter Array (ALMA) is a key observational facility to study high-redshift sources in the sub/millimeter bands. Due to its high angular resolution and sensitivity, it can precisely identify sub/millimeter sources (e.g., S. M. Stach et al. 2019).

The properties of AGNs in SMGs have been intensely studied over the past two decades. For instance, D. M. Alexander et al. (2005) investigated the X-ray properties of SMGs in the 2 Ms Chandra Deep Field North (CDF-N), using a spectroscopically identified SCUBA 850 μm sample with radio counterparts from S. C. Chapman et al. (2005; $S_{850\mu m} = 2.4$–17.4 mJy). They showed that the majority (15/20) of those radio-detected SCUBA galaxies host X-ray AGNs, from which a large fraction (12/15) are moderately/highly absorbed ($N_H \geqslant 10^{23}\,\mathrm{cm}^{-2}$). On the basis of the ALMA 26 arcmin^2 Survey of GOODS-S at One-millimeter (ASAGAO; B. Hatsukade et al. 2018), combined with the deepest 7 Ms Chandra X-ray survey, Y. Ueda et al. (2018) found that $90^{+8}_{-19}\%$ and $57^{+23}_{-25}\%$ of millimeter-selected galaxies with $L_{IR} > 10^{12}\,L_\odot$ and $10^{11}\,L_\odot < L_{IR} < 10^{12}\,L_\odot$ at $z = 1.5$–3 contain X-ray-detected AGNs. The GOODS fields were also studied by an ultradeep SCUBA-2 survey (a submillimeter perspective on the GOODS fields (SUPER GOODS); L. L. Cowie et al. 2017, 2018; A. J. Barger et al. 2019, 2022). As a study in a wider field with relatively shallow X-ray observations, S. X. Wang et al. (2013) studied SMGs in the Extended Chandra Deep Field South (E-CDF-S), utilizing the ALMA LABOCA-E-CDF-S Submillimeter Survey (ALESS; J. A. Hodge et al. 2013; $S_{870\mu m} = 1.3$–9.0 mJy). They identified eight X-ray AGNs from 91 SMGs in the shallower Chandra footprints, from which six sources are moderately/highly absorbed. Similarly, S. M. Stach et al. (2019) examined the properties of SMGs in the UKIDSS Ultra Deep Survey (UDS) field, based on the ALMA SCUBA-2 UDS survey (AS2UDS; S. M. Stach et al. 2018; $S_{870\mu m} = 0.6$–13.6 mJy). They found 23 X-ray AGNs from 274 SMGs in the shallow Chandra coverage. They also found 37 potential AGNs that were not detected in X-ray from 162 IRAC-selected SMGs at $z < 3$, utilizing the IRAC color selection of J. L. Donley et al. (2012). Moreover, studies of high-density regions by Y. Tamura et al. (2010) and H. Umehata et al. (2015, 2019) have investigated the properties of AGNs in a protocluster at $z = 3.09$ (SSA22). Although these studies constrained the physical properties of AGNs in SMGs, the derived values vary from study to study. For a more comprehensive understanding of the nature of AGNs in SMGs, it is necessary to study a larger sample and wider parameter ranges of SMGs.

The detection of AGNs in galaxy samples is always challenging. Historically, many studies used X-ray observations and/or optical spectroscopy to study the nature of AGNs. However, these methods have a bias against the most heavily obscured sources (see R. C. Hickox & D. M. Alexander 2018 for a review). In heavily obscured AGNs, X-ray and ultraviolet (UV) emission from the inner regions of the accretion disk around the SMBH is absorbed by surrounding material and is reemitted in the mid- to far-infrared bands. Color–color diagrams in the mid-infrared wave bands are able to identify such heavily obscured systems, but they are less reliable for high-redshift sources ($z > 3$; J. L. Donley et al. 2012) and lower-luminosity AGNs, where the mid-IR emission can be strongly contaminated by the host galaxy (see also A. Pope et al. 2008). Spectral energy distribution (SED) modeling of

broadband (rest-frame UV to far-infrared) photometries is a promising method to robustly identify hidden AGNs missed at X-ray and optical energies. Although this method is dependent on the quality of the multiwavelength photometry and model assumptions, it has successfully identified AGN candidates that are not detected in X-ray observations (e.g., C. Andonie et al. 2022; G. Yang et al. 2023; R. Uematsu et al. 2024; T. C. C. Chien et al. 2024; C.-L. Liao et al. 2024).

In this study, we investigate the properties of AGNs hosted by bright SMGs in the COSMOS field, utilizing the ALMA/SCUBA-2 COSMOS Survey (AS2COSMOS; J. M. Simpson et al. 2020). This survey is a follow-up of the brightest $\sim$180 submillimeter sources that were detected in the SCUBA-2 COSMOS Survey (S2COSMOS; J. M. Simpson et al. 2019) and is effectively complete for S2COSMOS sources brighter than $S_{850\,\mu m} = 6.2$ mJy. We perform rest-frame UV to far-infrared SED modeling for the AS2COSMOS SMG sample and identify AGNs. We also perform an X-ray spectral analysis of the bright X-ray-detected AGNs. On the basis of these results, we discuss the properties of the AGNs and their host galaxies. The structure of this paper is as follows: In Section 2, we describe the observations and data reduction. In Section 3, we describe the SED modeling and the X-ray spectral analysis. Section 4 presents our results and discussions. A summary is given in Section 5. Throughout the paper, we assume a flat universe with $H_0 = 70.4\,\mathrm{km\,s^{-1}\,Mpc^{-1}}$, $\Omega_M = 0.272$ (E. Komatsu et al. 2011). The Chabrier initial mass function (IMF) is adopted (G. Chabrier 2003). We use the AB magnitude system (J. B. Oke & J. E. Gunn 1983). If not specially mentioned otherwise, the quoted errors correspond to 1σ confidence.

2. Observations and Data Reduction

2.1. Submillimeter Photometry

The ALMA submillimeter source catalog that is the basis of our analysis was presented in J. M. Simpson et al. (2020). The pilot study of AS2COSMOS was performed in ALMA Cycle 4. This survey followed up 160 of the brightest SCUBA-2 850 μm sources in the COSMOS field from the S2COSMOS survey (J. M. Simpson et al. 2019), of which 158 had deboosted/deblended 850 μm flux densities of $S_{850\,\mu m} > 6.2$ mJy. Observations were conducted between 2018 May 15 and 21 covering the 7.5 GHz bandwidth centered at 343 GHz (870 μm; Band 7). Supplemented by the archival ALMA Band 7 imaging, J. M. Simpson et al. (2020) constructed a sample of 182 brightest S2COSMOS sources (deboosted/deblended flux densities of $S_{850\,\mu m} > 6.2$ mJy) with ALMA Band 7 imaging. All the ALMA data were calibrated and reduced with the Common Astronomy Software Applications (CASA) package (v5.1.1). The final images have a median synthesized beam size of $0.''80 \times 0.''79$ FWHM and a median sensitivity of $\sigma_{870\,\mu m} = 0.19$ mJy beam^{-1}.

Source extraction was performed with SExtractor. First, J. M. Simpson et al. (2020) extracted sources within the ALMA primary beams with a significance of $> 4.8\sigma$ at a peak or $> 4.9\sigma$ in an aperture with a 1.5 $\times$ FWHM of the synthesized beam. The number of false detections fell to zero with these criteria. In this step, J. M. Simpson et al. (2020) constructed a robust sample of 254 SMGs in 182 ALMA maps. Then, they extracted sources from the outer region of the ALMA primary beam with a slightly higher peak significance of $>5.1\sigma$, where
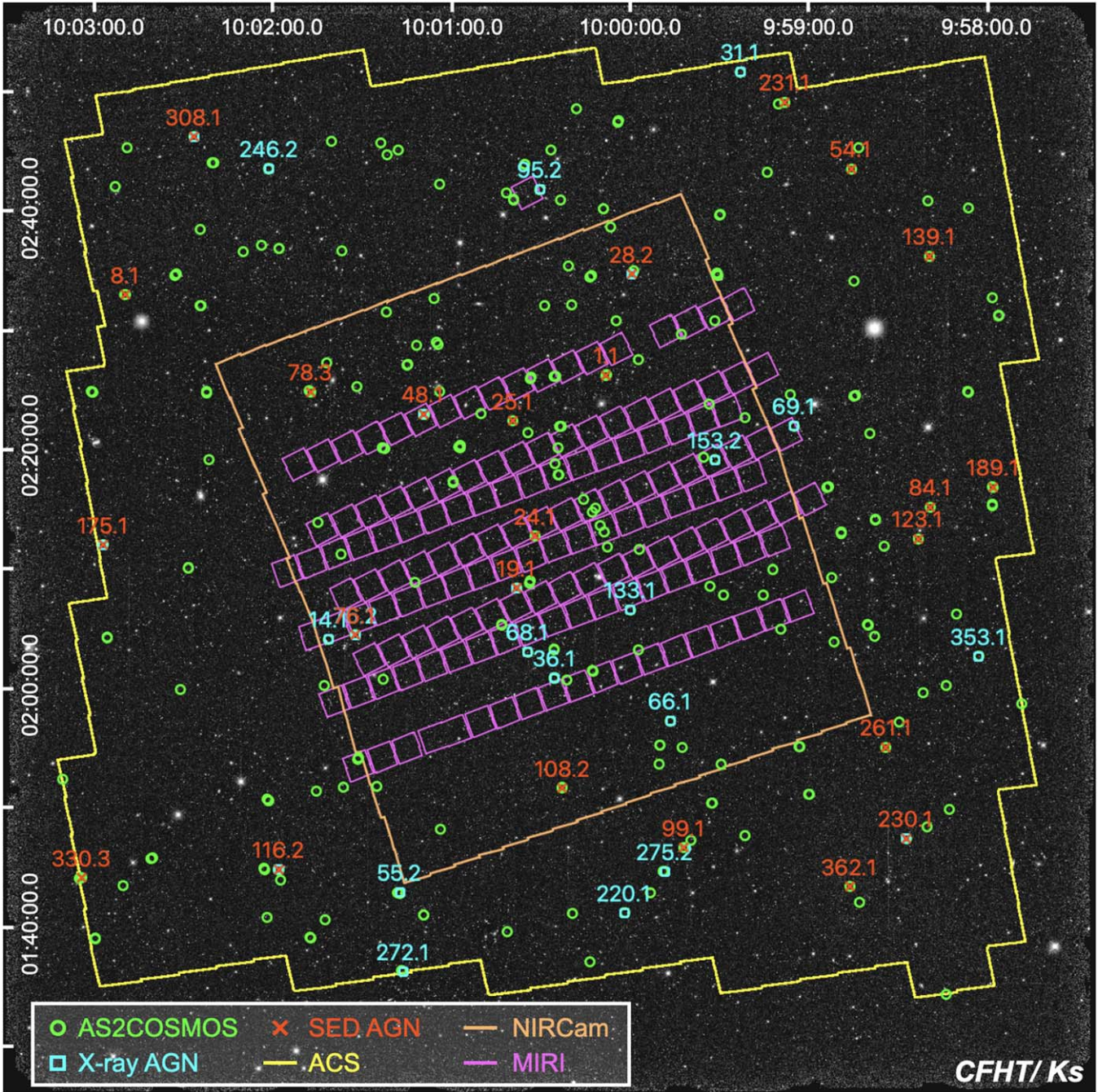
Figure 1. Positions of the AS2COSMOS sources. The cyan and red points correspond to the X-ray AGNs and SED AGNs, respectively (see Sections 3.1.3 and 4.1). The background is the CFHT K_s-band image. The coverage of Hubble Space Telescope (HST)/ACS, JWST/NIRCam, and JWST/MIRI imaging is shown in yellow, orange, and magenta, respectively.

the false detection rate again fell to zero. As part of this step, six additional SMGs were detected at $8\rlap{.}{''}9$–$11\rlap{.}{''}5$ offsets from the phase center. The final sample contains 260 SMGs out of the 182 brightest S2COSMOS sources. This sample effectively comprises all S2COSMOS sources brighter than $S_{850\,\mu m} = 6.2$ mJy. However, due to the influence of flux boosting on the SCUBA-2 catalog, this corresponds to an overall completeness of 50% for SMGs at $S_{850\,\mu m} = 7.2$ mJy in the 1.6 deg^2 survey area. We note that J. M. Simpson et al. (2020) confirmed a small astrometric offset of ΔR.A. $= 0\rlap{.}{''}08 \pm 0\rlap{.}{''}01$ between the AS2COSMOS and COSMOS2015 catalog (C. Laigle et al. 2016). In this study, we always correct

the source astrometry for this offset by referring to the COSMOS2015 catalog. Figure 1 shows the positions of the AS2COSMOS sources on a Canada–France–Hawaii Telescope (CFHT) K_s-band image.

2.2. Spectroscopic Redshifts

Spectroscopic redshifts of AS2COSMOS sources were obtained from several studies. We utilized the following spectroscopic surveys: the Sloan Digital Sky Survey (SDSS DR16; R. Ahumada et al. 2020), the zCOSMOS survey (DR3; S. J. Lilly et al. 2009), the VIMOS VLT Deep Survey (VVDS final data release; O. Le Fèvre et al. 2013), the PRIsm

MUlti-object Survey (PRIMUS DR1; A. L. Coil et al. 2011; R. J. Cool et al. 2013), the FMOS-COSMOS survey (version 2; J. D. Silverman et al. 2015; D. Kashino et al. 2019), the 3D-HST survey (R. E. Skelton et al. 2014; I. G. Momcheva et al. 2016), the Complete Calibration of the Color-Redshift Relation (C3R2) survey (DR3; D. C. Masters et al. 2019), the hCOSMOS survey (I. Damjanov et al. 2018), and the DEIMOS 10K spectroscopic survey (G. Hasinger et al. 2018). In addition to these catalogs, we used the results of the submillimeter line scan of the brightest AS2COSMOS sources performed by C.-C. Chen et al. (2022) and C.-L. Liao et al. (2024; see also J. E. Birkin et al. 2021). Moreover, we utilized the spectroscopic study of a galaxy cluster performed by T. Wang et al. (2016; AS2COS0003.1, AS2COS0003.2, AS2COS0003.3, and AS2COS0003.4) and the spectroscopic study of [C II] emitters performed by I. Mitsuhashi et al. (2021; (AS2COS0001.1, AS2COS0001.2, AS2COS0006.1, AS2COS0034.1, and AS2COS0034.2).

We cross-matched the AS2COSMOS sources with these catalogs within $1.''0$ radii and only used "secure" redshifts. With priority given to the submillimeter redshifts, 80 out of 260 sources had spectroscopic redshifts ranging from 0.033 to 5.3 (hereafter the "spec-z sample"). In Sections 3.1.1 and C.2, we show that the original optical counterpart of AS2COS0159.1 ($z_{\rm spec} = 0.033$) was misidentified. Therefore, the final spectroscopic redshift sample contains 79 SMGs within $z_{\rm spec} = 0.3$–5.3. For the other sources, we calculate their photometric redshifts by utilizing CIGALE to simultaneously treat redshift uncertainties (hereafter the "photo-z sample"; Section 3.1.2).

2.3. Size Measurement with ALMA

The typical synthesized beam of the ALMA 870 μm observations in AS2COSMOS from J. M. Simpson et al. (2020) was $\sim0.''8$ FWHM. Given that the characteristic sizes of the bright dust continuum emission SMGs are believed to be $\sim0.''2$–$0.''3$ FWHM (e.g., J. M. Simpson et al. 2015; S. Ikarashi et al. 2015, 2017; J. A. Hodge et al. 2016; S. Fujimoto et al. 2018; B. Gullberg et al. 2019), the coarse resolution of our observations would have made it challenging to measure reliable sizes for such compact sources in the image domain. However, the high signal-to-noise ratio (S/N) of our ALMA detections (median integrated S/N $\sim$ 30, with a range of 17–52) meant that it would be possible to obtain constraints on the size of the dust continuum emission in the brighter sources in our sample using a visibility-domain analysis, as has been demonstrated in the past (e.g., D. Iono et al. 2006; J. D. Younger et al. 2008; S. Ikarashi et al. 2015, 2017; B. Gullberg et al. 2019).

The ALMA dust continuum size measurements were undertaken by S. Ikarashi et al. (2025, in preparation) and followed the methodology described in S. Ikarashi et al. (2015), with the exception that they adopted a Sérsic $n = 1$ exponential disk profile (rather than a Gaussian profile used in that earlier work) as suggested by high angular resolution submillimeter imaging of SMGs in the literature (e.g., J. A. Hodge et al. 2016; S. Fujimoto et al. 2018; J. A. Hodge et al. 2019; B. Gullberg et al. 2019). The first step in their analysis was to remove any other significant sources (S/N $\geqslant 5$) from the ALMA map of the primary source whose size was being measured. This is necessary since the visibility-domain analysis assumes that there is only a single source in the map. To remove the secondary sources, these were modeled using

the CLEAN task in CASA, employing its scratch option. This involved masking the other sources and cleaning down to 1σ noise level, before subtracting the modeled source visibilities from the ALMA visibility data.

Then, uv–amplitude plots were constructed for each source, by shifting the phase center to the position of the source and measuring the circularized, average flux in each uv–distance bin. A single exponential disk light profile ($n = 1$) model was then fitted to the uv–amplitude plot to obtain the best-fit size as a circularized half-light radius, $R_{\rm circ,0.5}$. S. Ikarashi et al. (2025, in preparation) also tested the reliability of their size measurements by performing simulations that involved injecting mock sources with known light profiles and sizes into the real ALMA visibility data and measuring their sizes in the same manner as for the real sources. This provided robust estimates of the errors in our size measurements. To determine the final size for each source, S. Ikarashi et al. (2025, in preparation) assessed whether the reported size is measurable (or only provides a limit) given the claimed S/N and resulting size using these Monte Carlo simulations, which also provided appropriate uncertainties on the source size measurements.

2.4. Optical to Far-infrared Photometry

The optical to radio photometric catalog for the SMG counterparts was also constructed by J. M. Simpson et al. (2020), by updating the COSMOS2015 photometry catalog (C. Laigle et al. 2016) to include deeper observations in the critical optical and near-infrared bands. By cross-matching the AS2COSMOS sources with the COSMOS2015 catalog, 179/260 optical/near-infrared counterparts were identified within search radii of $0.''85$, where the possibility of a false match is estimated at $\sim$6.6%. After that, the $YJHK_s$-band photometry was replaced with those in DR4 of the Ultravista survey (H. J. McCracken et al. 2012), which is up to ~ 0.5 mag deeper than DR2 used in the COSMOS2015 catalog. Photometry was measured using $2''$-diameter apertures centered at the SMG positions. In addition, the $BVriz$ photometry of the COSMOS2015 catalog was replaced with the $grizY$ photometry in the second data release of the Hyper Suprime-Cam Subaru Strategic Program (HSC-SSP; H. Aihara et al. 2019) if available. HSC-SSP DR2 reached $\sim$1 mag deeper than the optical imaging used in the COSMOS2015 catalog, and 158/260 counterparts were identified within $0.''85$. In total, 199/260 optical/near-infrared counterparts are identified in this step.

To obtain mid-infrared photometry, the 3.6–8.0 μm images of the Spitzer Large Area Survey combined with Hyper Supreme-Cam (SPLASH; C. L. Steinhardt et al. 2014) were utilized. The images were reduced with IRACCLEAN (B.-C. Hsieh et al. 2012), where sources are deblended by referring to the stacked $zYJHK_s$ detection images and ALMA 870 μm source positions. The far-infrared imaging of the COSMOS field was provided by three large programs: the COSMOS-Spitzer program (24 μm; D. B. Sanders et al. 2007), the PACS Evolutionary Probe (PEP) survey (100 and 160 μm; D. Lutz et al. 2011), and the Herschel Multi-tiered Extragalactic Survey (HerMES; 250, 350, and 500 μm; S. J. Oliver et al. 2012). The "superdeblended" catalog (S. Jin et al. 2018), which contains deblended 24–160 μm photometry for K_s and 3 GHz–selected sources, was cross-matched to the SMGs to improve completeness at the 24–100 μm band, and photometry was also obtained by cross-matching the AS2COSMOS sources with the PACS/PEP survey catalog (D. Lutz et al. 2011).

Finally, 250–500 μm photometry was derived following the method described in A. M. Swinbank et al. (2014), where the Spitzer 24 μm, Very Large Array (VLA) 3 GHz, and ALMA 870 μm source positions were used to deblend the Herschel images.

The radio photometry was taken from the source catalog of the VLA-COSMOS 3 GHz Large Project (V. Smolčić et al. 2017). Cross-matching the AS2COSMOS sources with the VLA 3 GHz catalog, 191 counterparts were identified within 1″. Since two pairs of SMGs were confused in the 3 GHz map (AS2COS0051.1/.2 and AS2COS0228.1/.2), the CASA/IMFIT routine was applied to deblend the fluxes of these sources.

2.5. High-resolution Imaging with JWST

The COSMOS field was observed with the James Webb Space Telescope (JWST) through two Cycle 1 JWST treasury programs. The first was PRIMER (J. S. Dunlop et al. 2021), which provides a contiguous 144 arcmin^2 with NIRCam in eight filters (F090W, F115W, F150W, F200W, F277W, F356W, F444W, and F410M) and a noncontiguous 112 arcmin^2 with MIRI in two filters (F770W and F1800W). The second was COSMOS-Web (C. M. Casey et al. 2023), which provides a contiguous 0.54 deg^2 with NIRCam in four filters (F115W, F150W, F277W, and F444W) and a noncontiguous 0.18 deg^2 with MIRI in one filter (F770W). A total of 107/260 AS2COSMOS sources fall within the coverage of the NIRCam imaging, whereas 43/260 sources are in the MIRI coverage (Figure 1). We utilized the reprocessed images provided by the DAWN JWST Archive (DJA) and constructed the color-composite images of those sources. Figure 2 shows the color-composite images of the 107 AS2COSMOS sources in the NIRCam coverage. The color-composite images of the 40 AS2COSMOS sources in the coverage of both NIRCam and MIRI are shown in Figure 13 in Appendix A. In Section 3.3, we perform a morphological analysis using these images. Note that the near-infrared counterpart of AS2COSMOS0005.1 has distorted morphology, indicating that it is a strong gravitational lens (Y.-H. Hwang et al. 2021; J. Pearson et al. 2024; S. Jin et al. 2024). This is due to gravitational lensing by a foreground galaxy. Thus, we exclude AS2COSMOS0005.1 and AS2COS-MOS0005.2 in the following analysis.

2.6. X-Ray Observations

2.6.1. Observation Overview and Cross-matching

The COSMOS field was observed with the Chandra X-ray Observatory (M. C. Weisskopf et al. 2002) through two large programs. The first was the Chandra COSMOS survey (C-COSMOS; M. Elvis et al. 2009), which was conducted from 2006 November to 2007 June. This survey covered the central 0.5 deg^2 of the COSMOS field with an exposure time of ~ 160 ks and an outer 0.4 deg^2 area of ~ 80 ks. The second program was the Chandra COSMOS-Legacy survey (F. Civano et al. 2016), which was carried out from 2012 November to 2014 March. During this survey, the outer region of C-COSMOS was observed to a depth of ~ 160 ks, achieving an effective exposure of $\simeq 160$ ks over the central 1.5 deg^2 and of $\simeq 80$ ks in the outer 0.7 deg^2. The whole survey detected 4016 point sources to limiting depths of 2.2×10^{-16} erg s^{-1} cm^{-2}, 1.5×10^{-15} erg s^{-1} cm^{-2}, and 8.9×10^{-16} erg s^{-1} cm^{-2} in the 0.5–2.0 keV, 2.0–10.0 keV, and 0.5–10.0 keV bands, respectively.

Cross-matching the AS2COSMOS sources with the latest catalog by F. Civano et al. (2016), we identified 23 X-ray counterparts within a radius of 1″.4. Since F. Civano et al. (2016) reported that 95% of the X-ray sources used for the astrometry correction have their optical counterparts within 1″.4, we employed this value for the cross-matching radius (the total false matching rate is ~ 0.3 across the entire field).

In this study, we performed an X-ray spectral analysis for the X-ray-detected sources to derive their X-ray luminosities and line-of-sight absorption. We also estimated the X-ray luminosity upper bounds for X-ray-undetected SMGs assuming typical X-ray spectra of AGNs.[15] Details of the X-ray spectral analysis are described in Section 3.2. Here we reanalyzed all the X-ray data, consisting of 117 pointings, using the Chandra interactive analysis of observations software (CIAO V4.15; A. Fruscione et al. 2006) and the latest calibration database (CALDB V4.10.7). Note that AS2COS0353.2 was initially identified as an X-ray source that was later confirmed as the counterpart of AS2COS0353.1 by visual inspection (Appendix B).

2.6.2. Source Extraction

Before extracting X-ray spectra of the SMGs, we performed X-ray astrometric corrections for all the observations, following F. Civano et al. (2016). First, we reprocessed the data with chandra_repro script, employing the vfaint mode for ACIS background cleaning. Next, we performed source detection in each 0.5–7.0 keV image with wavdetect tool. The point-spread function (PSF) maps were created at the 39.3% encircled count fraction (ECF) radius, assuming a single power-law spectrum with a photon index of 1.4 and Galactic absorption of $N_H = 2.6 \times 10^{20}$ cm^{-2} (P. M. W. Kalberla et al. 2005). We employed a "2 sequence" of wavelet scales (i.e., 1, 1.414, 2, 2.828, 4, 5.656, 8, 11.314, and 16 pixels) and a false-positive probability threshold of 10^{-6}. Then, we corrected the astrometry using the HSC i-band-selected subsample (17–24 AB mag) of the COSMOS2020 catalog (J. R. Weaver et al. 2022). In this step, only secure sources whose significance is higher than 5σ and whose PSF size is smaller than 2 pixels ($\sim 1''$) were cross-matched with the reference within 1″.5. On average, 15 sources were used to perform reprojection in each image. Finally, we combined all the images using merge_obs script. To confirm the astrometric accuracy, we again performed source detection in the combined image with the wavdetect tool. In this step, the length scale was varied from 0″.5 to 16″ in steps of $\sqrt{2}$. The detailed analysis of the Chandra astrometry is summarized in Appendix B.

We then extracted the X-ray spectra using circular apertures centered at the X-ray source positions. Here we determined the X-ray source positions by the frame that has the sharpest PSF at the detected position. The aperture radii were set to the 80 ECF radius in each frame, but an upper limit was set to 5″.0 for sources that are detected over 3σ in the 0.5–7.0 keV band[16] and to 4″.0 for the others.[17] Background spectra were taken from annuli with inner and outer radii of 8″.0 and 25″.0, respectively, by masking any X-ray sources with circular regions with radii

---

[15] Here we use the term "upper bound" to describe the upper boundary of confidence intervals (see V. L. Kashyap et al. 2010).

[16] Here we used the S/Ns that were reported in F. Civano et al. (2016).

[17] AS2COS95.2 was detected over 3σ in the 0.5–7.0 keV band, but the upper limit on the extraction aperture was set to 4″.0 to avoid contamination from a nearby source.
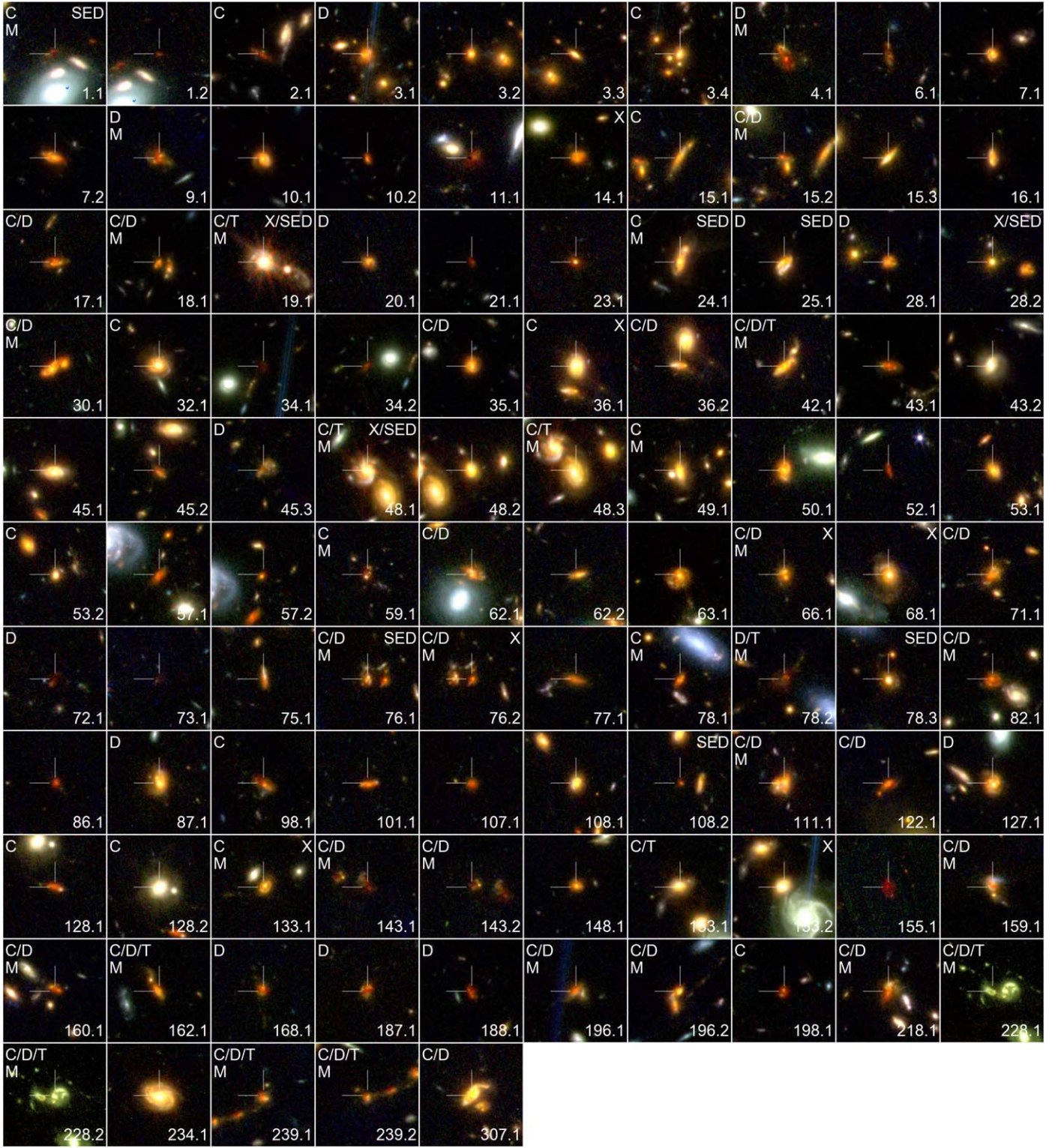
Figure 2. $8'' \times 8''$ JWST images of the 105 AS2COSMOS sources in the coverage of NIRCam (AS2COS0005.1 and AS2COS0005.2 are excluded). The blue, green, and red colors correspond to the F115W+F150W, F277W, and F444W filters, respectively. We label the merger candidates, which have tidal features (T), disturbed morphology (D), or possible companions (C) (see Section 3.3). The major merger candidates are indicated by "M." The X-ray AGNs and the SED AGNs are indicated by "X" and "SED" (see Section 3.1.3 and Section 4.1). Note that the images of AS2COS0107.1 and AS2COS0122.1 are constructed from F115W (blue), F277W (green), and F444W (red) filters, as they are not covered by F150W. For the same reason, the image of AS2COS0155.1 is constructed from F115W (blue), F2150W (green), and F277W (red), and those of AS2COS0228.1 and AS2COS0228.2 are constructed from F115W (blue), F115W+F150W (green), and F150W (red), respectively.

of $8''.0$. For X-ray-undetected SMGs, we estimated the X-ray upper bound count rates at 99.73% confidence intervals (3σ) in the 0.5–7.0 keV band, utilizing the SRCFLUX script. For the source regions, we employed circular apertures with radii of $3''.0$ centered at the $870\,\mu$m source positions. The background count rates were estimated by annular regions with inner and
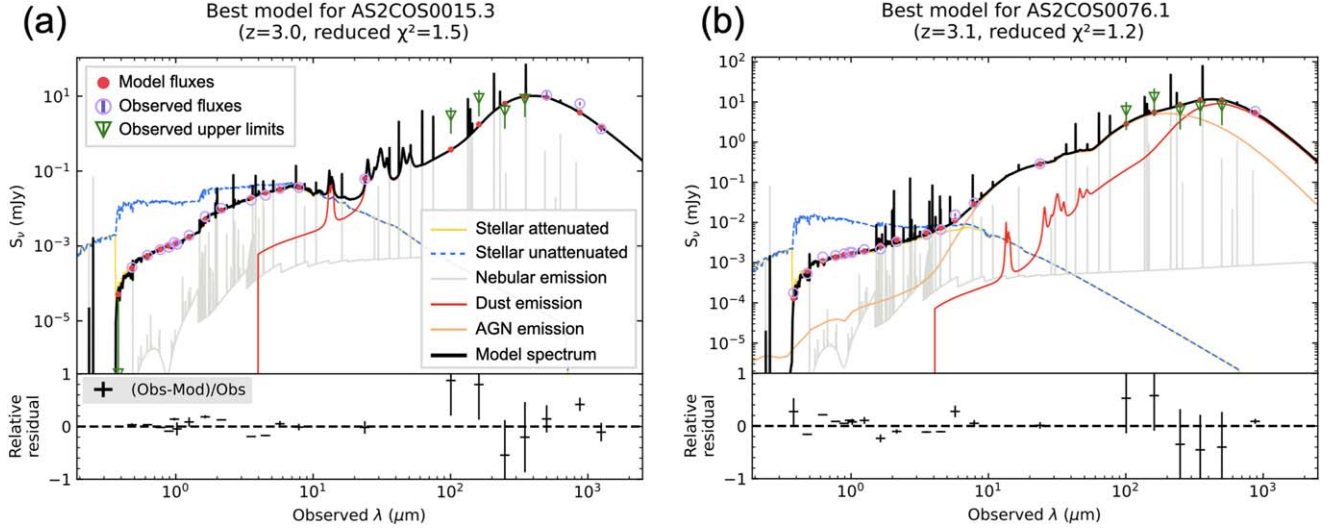
Figure 3. Example SEDs of a galaxy fitted (a) without and (b) with AGN templates. The black solid line represents the best-fit template SED solution. The yellow solid line illustrates the stellar emission attenuated by interstellar dust. The blue dashed line depicts the unattenuated stellar emission for reference. The orange line corresponds to the emission from the AGN. The red line shows the infrared emission from interstellar dust. The gray line denotes the nebula emission from the host galaxy. The observed data points are represented by purple circles, accompanied by 1σ error bars. The bottom panel displays the relative residuals between the best-fitting template solution and the photometry.

outer radii of $8''.0$ and $15''.0$, respectively, by masking any X-ray sources with circular regions with radii of $8''.0$.

3. Analysis

3.1. Optical to Submillimeter SED Analysis

3.1.1. SED Fitting

We perform optical to submillimeter SED modeling for the whole AS2COSMOS sample. We use CIGALE V2022.0 (M. Boquien et al. 2019; G. Yang et al. 2020, 2022), but incorporating modifications for the dust emission model as described below. The CIGALE code is designed to calculate the likelihoods of all the models on a user-defined grid and return the likelihood-weighted mean of the marginalized probability density function (pdf) as a Bayesian estimation. In CIGALE, users can choose several options for each SED component. We employ a delayed star formation history (SFH), accompanied by a recent starburst with a constant SFR. The composite stellar populations are calculated based on the stellar template of G. Bruzual & S. Charlot (2003) and the Chabrier IMF (G. Chabrier 2003). The dust extinction of the stellar component is modeled with the modified Calzetti starburst attenuation law (D. Calzetti et al. 2000; C. Leitherer et al. 2002; S. Noll et al. 2009). For the dust emission model, we use the ETHEMIS model (R. Uematsu et al. 2024), which is a high-temperature extension of the THEMIS model (A. P. Jones et al. 2017). The optical to far-infrared emission from an AGN is modeled with the SKIRTOR model (M. Stalevski et al. 2012, 2016), where a polar-dust component is implemented with a single optically thin graybody. The UV to optical emission from the accretion disk is modeled by a broken power law (M. Schartmann et al. 2005). In the SKIRTOR model, an AGN whose inclination angle is smaller (larger) than the half-opening angle of the torus is classified as a type 1 (type 2) AGN. We employ this classification in later sections.

In CIGALE, the number of parameter grid points is often limited by computational cost. Hence, we need to optimize the

parameter set to adequately reproduce the SEDs given this limitation. Moreover, there remain some possible errors in extracting photometry, such as remaining blending effects or calibration issues. For these reasons, we separate the SED modeling into two steps. In the first step, we analyze all the SEDs with a robust parameter set, which is summarized in Table 2 in Appendix C. In this step, we adequately reproduce most of the SEDs with reduced χ^2 values typically lower than 5. Then, in the second step, we reanalyze the remaining sources by optimizing the photometry or adjusting the parameter settings. Details of these iterations are summarized in Appendix C. With this approach, we adequately reproduce the SEDs of the AS2COSMOS sources (χ^2/degrees of freedom (dof) < 7; see Figure 16 in Appendix C). Figure 3 illustrates two example SEDs of AS2COSMOS sources fitted with and without AGN templates. Note that the radio component is not simultaneously treated in the SED modeling to save the computational cost.

When calculating the physical properties, we vary stellar mass (M_*), SFR, dust mass (M_{dust}), and infrared luminosity (L_{IR}) logarithmically,[18] while the following are varied linearly: dust temperature (T_{dust}), color excess of stellar continuum attenuation ($E(B-V)$), power-law index to modify the Calzetti attenuation slope (δ), AGN luminosity fraction in the total dust luminosity (f_{AGN}), bolometric AGN luminosity ($L_{AGN, bol}^{SED}$), and redshift (z). For SFR, we employ 10 Myr averaged values. The specific SFRs (sSFRs) are calculated by dividing the SFRs by the stellar masses. The radio−IR correlation parameters (q_{IR}) are calculated by the following equation:

$$q_{IR} = \log\left(\frac{L_{IR}}{L_{\nu,21\,cm} \times 3.75 \times 10^{12}\,Hz}\right). \quad (1)$$

The radio luminosity density at 21 cm is converted from the radio flux density at 3 GHz assuming a spectral index of 0.75

---

[18] In CIGALE, the infrared luminosity is calculated by the sum of the dust luminosity from the AGN and the dust luminosity from the host galaxy. This is almost the same as the integrated luminosity between 8 and 1000 μm.

(e.g., J. J. Condon 1992; E. Ibar et al. 2009, 2010). Note that the spectral index was reported to have large uncertainty (a standard deviation of 0.29; E. Ibar et al. 2010) and care should be taken. The SFR is directly calculated from the stellar templates, and this value corresponds to the sum of UV (unobscured) and far-infrared (obscured) SFRs.

3.1.2. Treatment of the Redshift Uncertainty

In the SED modeling, the redshifts of the SMGs without spectroscopic redshifts are allowed to vary within $0.1 < z < 6.0$ (photo-z sample). Hence, the physical quantities derived by CIGALE include the redshift uncertainties. However, in the X-ray spectral analysis, redshifts are always fixed at the spectroscopic redshifts or the Bayesian-estimated photometric redshifts derived by SED modeling (Section 3.2). This inconsistency can cause a problem in comparing the physical properties. Therefore, we repeat the SED modeling by fixing the redshifts at either the spectroscopic ones or the Bayesian-estimated photometric ones. The values estimated in this way are used for comparison with the X-ray properties.

3.1.3. Identification of AGNs

To identify whether a galaxy hosts an AGN or not, we utilize the Bayesian information criterion (BIC). The BIC is calculated as $BIC = \chi^2 + k \times \ln(n)$, where χ^2 is the nonreduced χ^2 value, k is the dof, and n is the number of photometric points. In this study, we regard the sources with $\Delta BIC = BIC_{w/o\ AGN} - BIC_{w/\ AGN} > 10$ as hosting AGNs (SED AGNs; see also Y. Toba et al. 2020). The median number of photometric points in the SED fitting is 21, and the dof for the AGN module is 4. Thus, this criterion roughly corresponds to the improvement in reduced χ^2 of 1. However, in some cases, this method gives unreasonable results, due to the limited parameter range of the SED model. Thus, we also visually examine the SEDs and conclude that there is no evidence of AGNs in the SED of AS2COS0001.2, where both mid-infrared excess and a flat far-infrared SED are not confirmed. Finally, we identify 24 SED AGNs in the AS2COSMOS sample, where seven sources are also detected in X-ray.

Figure 4 shows the histogram of ΔBIC. Notably, most of the X-ray-detected sources (16 out of 23) exhibit BICs lower than 10. This shows that the SED AGNs provide a complementary AGN sample to the X-ray AGNs in our sample (see Section 4.1). In addition, all three type 1 SED AGNs (AS2COS0019.1, AS2COS0175.1, and AS2COS0230.1) are detected in X-ray, which is consistent with the unobscured nature of those systems. We emphasize that this method strongly depends on the quality of the multiwavelength photometry and model assumptions. In particular, at high redshift ($z \geqslant 3$) or in optical(/near-infrared)-dark systems, the indicators of AGNs are sometimes limited to a slight excess at observed-frame 24 μm flux density or relatively flat SED at observed-frame 100–1000 μm, which are difficult to distinguish from the polycyclic aromatic hydrocarbon (PAH) emission from the host-galaxy dust or hot dust emission associated with a starburst. In our SED AGN sample, the evidence for AGNs in AS2COS0025.1, AS2COS0084.1, AS2COS0099.1, AS2COS0108.2, and AS2COS0330.3 appears to be fairly limited, and we should be careful of these sources. For sources other than the SED AGNs, we estimate the
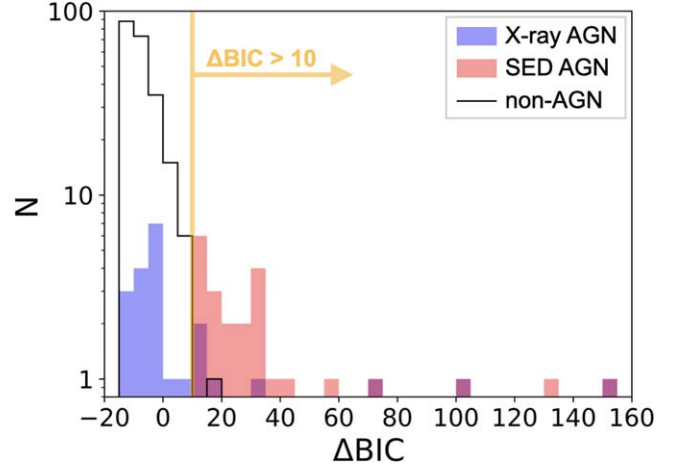

Figure 4. Distribution of ΔBIC of the X-ray-detected AS2COSMOS sources (X-ray AGNs; see Section 4.1), SED AGNs, and all the AS2COSMOS sources. The vertical orange solid lines show the adopted threshold to identify an SED AGN ($\Delta BIC = 10$). Most of the X-ray-detected sources (16 out of 23) have BICs lower than 10, suggesting that the SED AGNs are the complementary sample to X-ray-detected AGNs.

99.73% (3σ) upper bound of the bolometric AGN luminosity by integrating the marginalized pdf's with a uniform prior. Except for the SED AGNs, the physical properties of the galaxies are calculated without the AGN component.

3.1.4. SED Modeling Check

For a consistency check, we compare some observational properties with the physical properties derived by the SED modeling that they are expected to most strongly correlate with. Figure 17 in Appendix D presents these comparisons. We confirm a strong correlation between dust mass and 870 μm flux density as reported in U. Dudzevičiūtė et al. (2020). Additionally, we confirm that the 5.8 μm flux density, which corresponds to the rest-frame H-band flux density at the median redshift of $z = 2.47$, shows a positive correlation with the stellar mass. Moreover, the photometric redshifts derived by CIGALE are reasonably correlated with the spectroscopic redshifts; the median difference and the standard deviation are $\Delta z/(1 + z) = (z_{photo} - z_{spec})/z_{spec} = -0.04 \pm 0.19$. Note that the photometric redshifts derived by CIGALE are also reasonably aligned with those derived by EAZY and LEPHARE, which are listed in the COSMOS2020 catalog; the median differences and the standard deviations are $\Delta z/(1 + z) = (z_{eazy/lephare} - z_{cigale})/z_{cigale} = 0.14 \pm 0.62$ for EAZY and 0.09 ± 0.41 for LEPHARE. Determining the physical properties of galaxies with SED analysis is sometimes challenging or unreliable, particulary for a type 1 SED AGN, where the AGN emission can mask the host-galaxy emission. To address this issue, we perform a mock analysis, which is a procedure provided by CIGALE (see Section 4.3 in M. Boquien et al. 2019), for all the AS2COSMOS sources (Appendix E). The median differences and the standard deviations are $\Delta \log SFR = \log SFR(mock) - \log SFR = -0.01 \pm 0.19$ and $\Delta \log M_* = \log M_*(mock) - \log M_* = 0.02 \pm 0.19$.

To validate our AGN selection, we compare the properties of our sources to the conventional AGN selection using a color–color diagram in the mid-infrared bands. Figure 5(a) displays the mid-infrared color–color diagram of the AS2COSMOS
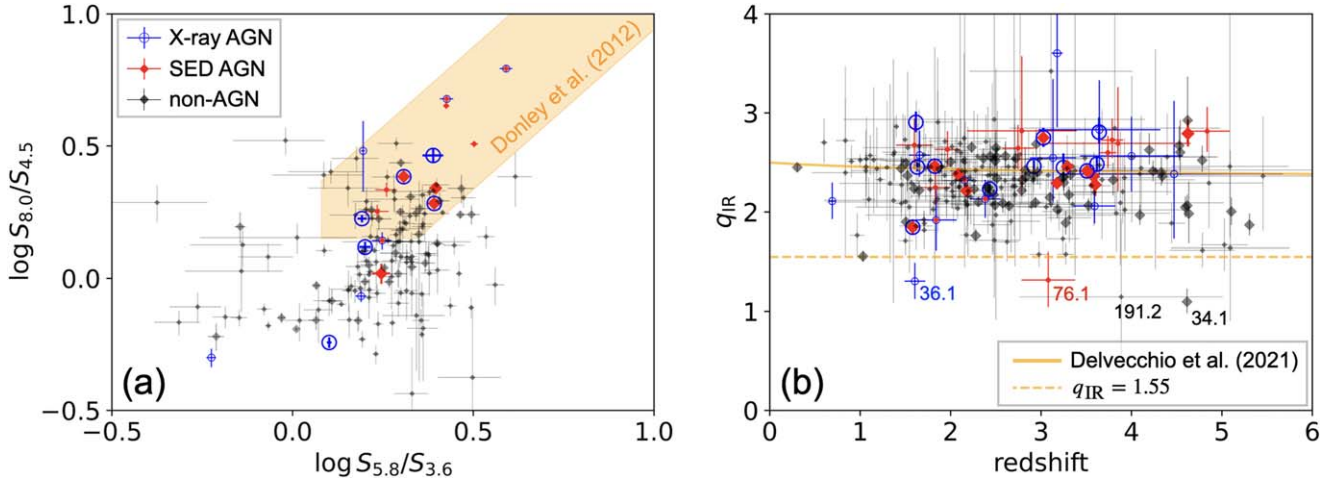
Figure 5. (a) Mid-infrared color–color diagram of the AS2COSMOS sources. The shaded area shows the AGN selection criteria by J. L. Donley et al. (2012). Note that only the sources that are detected in all the mid-infrared bands (Spitzer 3.6, 4.5, 5.8, and 8.0 μm) are plotted in this figure. Moreover, the sample is limited to $z < 3$, where the selection criteria by J. L. Donley et al. (2012) are applicable. We confirm that most of the SED AGNs meet the AGN criteria by J. L. Donley et al. (2012). (b) Distribution of q_{IR} as a function of redshift. The solid line illustrates the empirical relation of star-forming galaxies at $M_* = 10^{11} M_\odot$ (I. Delvecchio et al. 2021), while the dashed line indicates $q_{IR} = 1.55$, which is used as the threshold of radio-excess AGNs in H. S. B. Algera et al. (2020). The large symbols show the spec-z sample, while the smaller ones show the photo-z sample. We confirm that most of the AS2COSMOS sources follow the empirical relation of star-forming galaxies, while two AGNs and two non-AGNs show radio-loud characteristics.

sources. The orange area denotes the AGN criteria by J. L. Donley et al. (2012). Note that only the sources detected in all the mid-infrared bands (Spitzer 3.6, 4.5, 5.8, and 8.0 μm) are plotted in this figure. We also limit the sample to $z < 3$ because the stellar emission can produce a similar shape to the AGN emission at high redshift (J. L. Donley et al. 2012). We confirm that 9/11 of the SED AGNs are located in the AGN region, while two SED AGNs (AS2COS0025.1 and AS2COS0230.1) are not. AS2COS0025.1 shows a possible excess in the Spitzer 24 μm band, which appears to drive the AGN classification. AS2COS0230.1 has a flat rest-frame optical SED, which may favor the presence of an AGN.

A significant fraction of galaxies in the AGN region (40/49) are not classified as hosting AGNs by the BIC selection. A total of 24 out of these 40 AGN-unclassified galaxies in the AGN region have relatively high redshifts ($z \gtrsim 2.4$), which may make it difficult to distinguish AGN-host galaxies from DSFGs in the mid-infrared color–color diagram (S. M. Stach et al. 2019). The CIGALE fits for the other 13 sources with lower redshift ($1.0 \lesssim z \lesssim 2.0$) are suggested to have strong 3.3 μm PAH emission, which may have caused the misidentification in the mid-infrared color–color diagram. However, we need to consider the possibility that the near-infrared AGN emission is misidentified as the 3.3 μm PAH emission in the SED fitting. The remaining three sources lie near the edge of the selection criteria. In summary, we conclude that the AGN selection by BIC provides a more conservative sample of SED AGNs than the conventional selection using the mid-infrared color–color diagram at $z < 3$.

We also check the radio-loudness of the SMGs. Figure 5(b) plots the radio–IR correlation factors as a function of redshift. The solid and dashed lines denote the empirical relation of star-forming galaxies at $z = 0$–4 (I. Delvecchio et al. 2021) and a criterion for radio-excess AGNs ($q_{IR} \leqslant 1.55$; H. S. B. Algera et al. 2020), respectively. We confirm that our sample mostly aligns with the empirical relation of star-forming galaxies. One X-ray-detected AS2COSMOS source and an X-ray-undetected SED AGN have especially low radio–IR correlation factors ($q_{IR} = 1.3 \pm 0.2$ and 1.3 ± 0.3 for AS2COS0036.1 and

AS2COS0076.1, respectively), suggesting that these sources are radio-excess AGNs. Two galaxies that are not detected in X-ray or identified as SED AGNs also have low radio–IR correlation factors ($q_{IR} = 1.1 \pm 0.2$ and $1.1^{+0.8}_{-0.7}$ for AS2COS0034.1 and AS2COS0191.2, respectively). This might suggest that they are candidates for radio-excess AGNs. These sources are located at high redshift, which may have made it difficult to identify AGNs by SED modeling. In total, the AS2COSMOS sample contains 4/258 ($1.5^{+1.2}_{-0.7}$%) radio-excess sources. This fraction is consistent with the previous studies of the AS2UDS sample (12/659, 1.8% $\pm$ 0.5%; H. S. B. Algera et al. 2020).

The 18 brightest and not strongly lensed AS2COSMOS sources ($S_{870~\mu m} = 12.4$–19.2) were also analyzed in C.-L. Liao et al. (2024). They performed X-ray to radio SED modeling with CIGALE and found that the luminosity fractions of AGNs in the total infrared luminosities (f_{AGN}) are always lower than $\sim$10% in their sample. However, in our study some of these sources have moderately high AGN luminosity fraction ($f_{AGN} = 0.56 \pm 0.13$, 0.38 ± 0.05, 0.55 ± 0.13, and 0.49 ± 0.03 for AS2COS0001.1, AS2COS0008.1, AS2COS0054.1, and AS2COS0139.1, respectively), indicating significant contributions of AGNs in those systems. These inconsistencies can be attributed to the different parameter settings used for CIGALE. In particular, since the radio photometry of some of the AS2COSMOS sources has a high S/N, the radio-loudness parameter can sometimes behave as the normalization for the AGN component. In C.-L. Liao et al. (2024), the radio-loudness parameter was sampled at 1 dex intervals in the fitting. Thus, f_{AGN} might not be estimated with an accuracy of less than 1 dex, which might cause potential trouble in the identification of AGNs. In addition, care needs to be taken about the possible degeneracies between the parameters in SED modules. For example, the host-galaxy dust emission module has a potential degeneracy with the AGN module. Thus, if we limit the parameter range of the host-galaxy dust emission module, the contribution of the AGN module can be overestimated. Currently, we are not able to calculate all the possible parameter grids and test the degeneracies between the SED modules owing to the computational cost. Future studies on the SED modules themselves are needed to solve this problem.

3.1.5. Selection Bias of SED AGNs

Detection of type 2 AGNs using SED modeling mostly occurs as a result of the dominance of AGN emission in the infrared bands. Consequently, it is more difficult to identify an AGN in a strongly star-forming galaxy because the host-galaxy emission will mask the emission from the AGN (see also C. Andonie et al. 2022). This selection can be characterized by the AGN luminosity fraction in the total infrared luminosity ($f_{\rm AGN}$). In our sample, the type 2 SED AGNs have $f_{\rm AGN}$ larger than ~0.3, which is considered to be the detection limit of the SED AGNs in our study. Assuming a typical SED of a type 2 AGN and the tight SFR–$L_{\rm IR}$ correlation, this detection limit can be expressed as follows:

$$
\begin{aligned}
{\rm SFR}\ [M_\odot\ {\rm yr^{-1}}] &\gtrsim \frac{1-f_{\rm AGN}}{f_{\rm AGN}} \times \kappa_{\rm IR}^{-1} \times L_{\rm AGN,\,bol}\ [{\rm erg\ s^{-1}}] \\
&\quad \times \kappa'_{\rm IR} \\
&= 4.2 \times 10^{-44} \times L_{\rm AGN,\,bol}\ [{\rm erg\ s^{-1}}], \quad (2)
\end{aligned}
$$

where $\kappa_{\rm IR}$ is the infrared to bolometric correction factor of an AGN and $\kappa'^{-1}_{\rm IR}$ is the conversion factor of infrared luminosity to SFR. Here we assume $\kappa_{\rm IR} = 1.6$, which is calculated by the SKIRTOR model with $\tau_{9.7} = 7$, $p = 1$, $q = 1$, $\Delta = 40°$, $R = 20$, $\theta = 70°$, $E(B - V) = 0.1$, and $T_{\rm pol} = 100$ K. For $\kappa'_{\rm IR}$, we employ the calibration by R. C. J. Kennicutt (1998), where a factor of 0.63 is applied to convert Salpeter IMF to Chabrier IMF. Note that this detection limit is not as applicable to type 1 AGNs because type 1 AGNs can also be selected by their flat UV to optical spectra. Moreover, the detection of AGNs by SED modeling is expected to have a potential bias against high-redshift ($z > 3$) AGNs unless 24 μm flux densities are available, since the hot dust emission from an AGN is redshifted out of the mid-infrared bands (3.6–8.0 μm) and can only be identified by the 24 μm flux density.

3.2. X-Ray Analysis

3.2.1. X-Ray Spectral Analysis for X-Ray-detected Sources

We perform an X-ray spectral analysis of the X-ray-detected AS2COSMOS sources. To appropriately treat the low-count statistics, we use the C-statistic (W. Cash 1979). We first construct a background model utilizing the combined background spectrum. We employ an analytical model referring to H. Suzuki et al. (2021), but including a simplification to avoid unreasonable fits. The background model used in this study is expressed as follows in the XSPEC terminology (K. A. Arnaud 1996):

$$
\begin{aligned}
{\rm model\_back} = &\ {\tt gaussian + gaussian + gaussian} \\
&+ {\tt gaussian + gaussian + gaussian} \\
&+ {\tt gaussian + gaussian + gaussian} \\
&+ {\tt gaussian} \\
&+ {\tt powerlaw + gabs*expdec.}
\end{aligned}
$$
$$(3)$$

The nine Gaussian lines represent the fluorescence lines from the instrument: Al Kα (1.487 keV), Al Kβ (1.557 keV), Ni Kα (7.478 keV), Ni Kβ (8.265 keV), Au Mα (2.123 keV), Au Mβ (2.205 keV), Au Mγ (2.410 keV), Au Lα_1 (9.713 keV), and Au Lα_2 (9.628 keV). The widths of these lines are fixed at 1 eV. The remaining Gaussian line corresponds to the broad-line

component at 2.7 keV produced by the inappropriate correction of charge transfer inefficiency. The continuum background spectrum is approximated by a power law and an exponential decay with Gaussian profile absorption. We note that this model is not multiplicated by the ancillary response file, assuming that the background spectrum is dominated by particle-induced events. We confirm that this model adequately reproduces the combined background spectrum (C-statistic = 826 for 634 dof). The best-fit parameters are summarized in Table 4 in Appendix F. In the later sections, we fix the parameters except for the normalizations of additive components, which are left as free parameters to treat the slight differences among the observations.

Adopting this approach, we simultaneously fit the source and the background spectra. Here we assume that the source X-ray spectra are dominated by AGN emission. The X-ray spectrum of an AGN is approximated to three components: (1) a direct component from the nucleus, (2) reflection components from the torus and/or the accretion disk, and (3) a scattered component with emission from the photoionized plasma. The photoionized emission is usually much fainter than the direct or reflection components at rest-frame energies above 2.0 keV. Thus, we do not consider this component in the spectral analysis. The reflection from an accretion disk is also excluded because its contribution to the X-ray spectrum is still under debate (S. Ogawa et al. 2019, 2021). The combined spectrum is expressed as follows in the XSPEC terminology:

$$
\begin{aligned}
{\rm model\_source} = &\ {\tt phabs*(zphabs*cabs*zcutoffpl} \\
&+ {\tt const*zcutoffpl} \\
&+ {\tt atable\{xclumpy\_v01\_RC.fits\}} \\
&+ {\tt atable\{xclumpy\_v01\_RL.fits\}).}
\end{aligned}
$$
$$(4)$$

The first factor represents the galactic absorption, which is calculated following the method of R. Willingale et al. (2013). The first term in parentheses represents the direct component. The second term corresponds to the unabsorbed scattered component. The third and fourth terms are the reflection component from the torus. In this study, we employ the XCLUMPY model, which reproduces the X-ray reflection from a clumpy torus (A. Tanimoto et al. 2019). The photon index, cutoff energy, and normalization of the reflection and scattered components are linked to those of the direct component. The line-of-sight hydrogen column density ($N_{\rm H,X}^{\rm LOS}$) of the direct component is set to be consistent with the torus geometry (see Equation 3 in A. Tanimoto et al. 2019). Redshifts are fixed at the spectroscopic ones or the Bayesian-estimated values derived by the SED modeling. Because of the modest data quality, the scattered fraction, photon index, and cutoff energy are fixed at 0.01, 1.9, and 370 keV, respectively. Note that the photon index is confirmed to be unconstrained except for AS2COS0019.1, where AS2COS0019.1 has fits in which a photon index of 1.9 lies within the 90% confidence interval. Moreover, the torus angular width (σ) and the equatorial hydrogen column density ($N_{\rm H,X}^{\rm Equ}$) are fixed at 20° and 10^{25} cm^{-2}, respectively. Finally, the free parameters in the X-ray spectral fitting are the inclination angle (i; 18°–87°), which is linked to the line-of-sight hydrogen column density, and the normalization of the direct component.
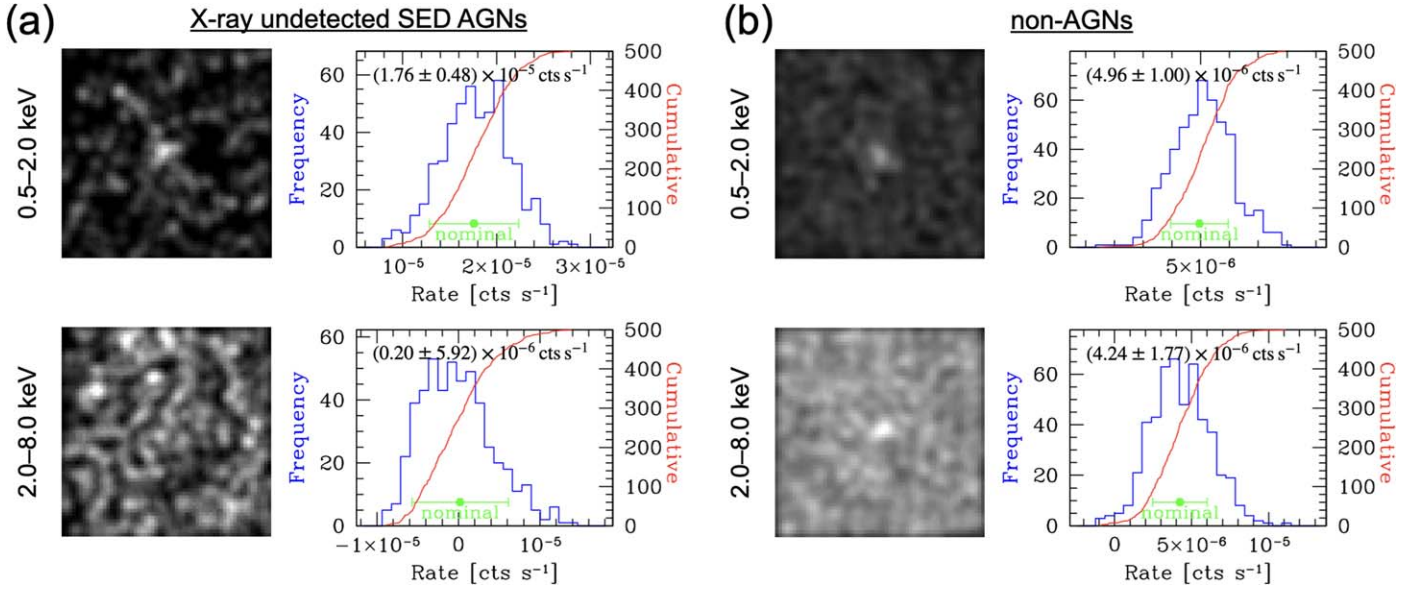
Figure 6. Results of X-ray stacking analysis for (a) the X-ray-undetected SED AGNs and (b) the other X-ray-undetected AS2COSMOS sources. The left panels show the stacked X-ray images, while the right panels show the bootstrap histograms of the net count rates. The mean count rates and the confidence intervals are shown in green and also reported in the histograms. Both samples are detected in the soft band (0.5–2.0 keV) over 3σ.

With this approach, we successfully reproduce the X-ray spectra of the 23 X-ray-detected sources with an AGN model (C-statistic < 1140 for 1285 dof). The X-ray spectra and the plots of the goodness of fit as a function of the line-of-sight hydrogen column densities are summarized in Appendix G. We confirm that all the sources have solutions in the Compton-thin regime ($N_{\mathrm{H,X}}^{\mathrm{LOS}} < 10^{24.2}$ cm^{-2}), with 12/23 sources showing significant absorption ($N_{\mathrm{H,X}}^{\mathrm{LOS}} > 10^{22}$ cm^{-2}). Note that seven SED AGNs are detected in X-rays, three of which are classified as type 1 and four of which are classified as type 2 from the SED analysis. All the X-ray-detected type 2 SED AGNs show significant absorption ($N_{\mathrm{H,X}}^{\mathrm{LOS}} > 10^{22}$ cm^{-2}), and two of the X-ray-detected type 1 SED AGNs do not. This shows the consistency of the X-ray analysis and the SED analysis of these sources. However, AS2COS0019.1 shows significant absorption in X-rays ($\log N_{\mathrm{H,X}}^{\mathrm{LOS}}/\mathrm{cm}^{-2} = 22.4_{-0.2}^{+0.1}$), while it is classified as a type 1 SED AGN. This might be attributed to the time variability of the AGN or the uncertainties associated with the model assumptions. AS2COS0036.1, AS2COS0055.2, AS2COS0066.1, AS2COS0076.2, AS2COS0095.2, AS2COS0153.2, AS2COS0220.1, and AS2COS0275.2 present alternative solutions in the Compton-thick regime that are not distinguishable from the Compton-thin solutions at a 90% confidence level. In later sections, we investigate these solutions separately to consider both possibilities. For the Compton-thick case, we calculate the X-ray luminosities by fixing the line-of-sight hydrogen column density[19] to $N_{\mathrm{H,X}}^{\mathrm{LOS}} = 9.8 \times 10^{24}$ cm^{-2}. The X-ray luminosities are calculated by correcting the line-of-sight absorption and the reflection from the torus. The median X-ray luminosity is estimated as $L_{2-10\,\mathrm{keV}} = 2.6 \times 10^{44}$ erg s^{-1} cm^{-2} for the Compton-thin cases and $L_{2-10\,\mathrm{keV}} = 3.1 \times 10^{45}$ erg s^{-1} cm^{-2} for the Compton-thick cases. Note that the X-ray spectral analysis of the sources in the COSMOS field is also performed by B. Laloux et al. (2023). We confirm that our estimations of

the line-of-sight hydrogen column densities and the X-ray luminosities are almost consistent with those in B. Laloux et al. (2023) within the errors.

3.2.2. Upper Bound Estimation for X-Ray-undetected Sources

For X-ray-undetected SED AGNs (Section 3.1), we convert the 3σ upper bound count rates to the intrinsic X-ray luminosities by assuming a typical AGN spectrum. We employ the same model as in Section 3.2.1, but the inclination angle is fixed to either $i = 47°$ ($N_{\mathrm{H,X}}^{\mathrm{LOS}} = 10^{23}$ cm^{-2}) or $i = 60°$ ($N_{\mathrm{H,X}}^{\mathrm{LOS}} = 10^{24}$ cm^{-2}) assuming Compton-thin absorptions. We also calculate the Compton-thick case by fixing the inclination angle to $i = 87°$ ($N_{\mathrm{H,X}}^{\mathrm{LOS}} = 9.8 \times 10^{24}$ cm^{-2}). Note that all the type 1 SED AGNs are detected with X-rays, so the X-ray upper bounds are only calculated for type 2 AGNs. The X-ray luminosities are calculated by correcting the line-of-sight absorption and the reflection from the torus. The median X-ray luminosity upper bound is estimated as $L_{2-10\,\mathrm{keV}} = 1.5 \times 10^{44}$ erg s^{-1} cm^{-2} for $N_{\mathrm{H,X}}^{\mathrm{LOS}} = 10^{23}$ cm^{-2}, $L_{2-10\,\mathrm{keV}} = 6.5 \times 10^{44}$ erg s^{-1} cm^{-2} for $N_{\mathrm{H,X}}^{\mathrm{LOS}} = 10^{24}$ cm^{-2}, and $L_{2-10\,\mathrm{keV}} = 4.7 \times 10^{45}$ erg s^{-1} cm^{-2} for $N_{\mathrm{H,X}}^{\mathrm{LOS}} = 10^{25}$ cm^{-2}.

3.2.3. Stacking Analysis of X-Ray-undetected Sources

We conduct an X-ray stacking analysis for the X-ray-undetected AS2COSMOS sources, using CSTACK V4.5 (T. Miyaji et al. 2008) with default settings for the maximum off-axis angle, the source region radius, and the exclusion of obvious X-ray sources. We separately stack the 17 X-ray-undetected SED AGNs and the 220 AS2COSMOS sources that are neither detected in X-rays nor identified as SED AGNs (non-AGNs). Figure 6 shows the results. Both samples are detected over 3σ in the soft band (0.5–2.0 keV) but not in the hard band (2.0–8.0 keV). The mean count rate of the X-ray-undetected SED AGN sample is about three times higher than that of the non-AGN sample. This might show the weak X-ray emission from the X-ray-undetected SED AGNs. However, given that the median far-infrared luminosity of the

---

[19] This is the hard limit of the XCLUMPY model (v1).

X-ray-undetected SED AGN sample is also about three times higher than that of the non-AGN sample, the difference does not necessarily trace the X-ray emission associated with the AGN activity. Moreover, the non-AGN sample is marginally detected in the 2.0–8.0 keV band (2.4σ), although the significance is not high. The inferred spectral shape is quite hard (photon index of ~ 1), implying a significant absorption of these sources ($N_{\rm H,X}^{\rm LOS} \sim 7 \times 10^{22}$ cm^{-2} for the AGN model in Section 3.2.1 at the median redshift of $z = 2.45$). This provides marginal evidence for the existence of obscured AGNs in the non-AGN sample.

Utilizing the integrated count rate derived from our stacking analysis, we calculate the typical X-ray luminosity of the X-ray-undetected SED AGN sample. Here we assume the same X-ray spectral model as in Section 3.2.2 placed at the median redshift of the X-ray-undetected SED AGN sample ($z = 3.18$). Since all these AGNs are classified as type 2 (see Section 3.1.1), we set the inclination angle at either $i = 47°$ ($N_{\rm H,X}^{\rm LOS} = 10^{23}$ cm^{-2}) or $i = 60°$ ($N_{\rm H,X}^{\rm LOS} = 10^{24}$ cm^{-2}) assuming Compton-thin absorption. However, considering that the stacked X-ray-undetected SED AGN sample is detected only in the soft band, we explore an unobscured AGN scenario by setting the inclination angle to $i = 15°$ ($N_{\rm H,X}^{\rm LOS} = 10^{20}$ cm^{-2}). In addition, we examine a Compton-thick scenario by fixing the inclination angle to $i = 87°$ ($N_{\rm H,X}^{\rm LOS} = 9.8 \times 10^{24}$ cm^{-2}). With this recipe, we estimate the stacked X-ray luminosity of the X-ray-undetected SED AGNs as $L_{2–10\,\rm keV} = (1.5 \pm 0.4) \times 10^{43}$ erg s^{-1} for $N_{\rm H,X}^{\rm LOS} = 10^{20}$ cm^{-2}, $L_{2–10\,\rm keV} = (2.4 \pm 0.7) \times 10^{43}$ erg s^{-1} for $N_{\rm H,X}^{\rm LOS} = 10^{23}$ cm^{-2}, and $L_{2–10\,\rm keV} = (2.4 \pm 0.6) \times 10^{44}$ erg s^{-1} for $N_{\rm H,X}^{\rm LOS} = 10^{24}$ cm^{-2} and $L_{2–10\,\rm keV} = (1.1 \pm 0.3) \times 10^{45}$ erg s^{-1} for $N_{\rm H,X}^{\rm LOS} = 9.8 \times 10^{24}$ cm^{-2}. Moreover, we evaluate the X-ray luminosity due to star formation activity from the integrated count rate of the non-AGN sample. In this calculation, we employ a power-law spectrum with a photon index of 2.1 (S. Sazonov & I. Khabibullin 2017) placed at the median redshift of $z = 2.45$. The stacked X-ray luminosity of the non-AGNs is estimated as $L_{2–10\,\rm keV} = (2.3 \pm 0.5) \times 10^{42}$ erg s^{-1}.

3.3. Morphological Study

Utilizing high-resolution imaging with JWST, we investigate the visual morphology of the 105/258[20] AS2COSMOS sources in the coverage of NIRCam imaging (see also J. McKinney et al. 2024 for a similar morphological study in COSMOS). We follow the same approach as the previous study of bright SMGs in the PRIMER region by S. Gillman et al. (2024). We assess the presence of distorted morphology, asymmetric structures, or tidal features by the color-composite images of the F115W, F150W, F277W, and F444W bands. Additionally, we check for the presence of possible companions in the F444W images. We classify sources with strongly disturbed morphology, tidal features, or potential bright companions (within a factor of four brightness of the target galaxy) as "major" merger candidates. Sources with less disturbed morphology or fainter companions are classified as "minor" merger candidates. The color-composite images of the 105 AS2COSMOS sources in the coverage of NIRCam are summarized in Figure 2. We identify 62/105 (59^{+5}_{-6}%) as potential merger candidates, from which 33/105 ($31\% \pm 5\%$) are classified as major mergers. These fractions are

broadly consistent with the previous work by S. Gillman et al. (2024). Note that we find six systems where both of the merging galaxies are included in the AS2COSMOS sample (AS2COS0036.1/36.2, AS2COS0048.1/48.3, AS2COS0076.1/76.2, AS2COS0143.2/143.2, AS2COS0228.1/228.2, and AS2COS0239.1/239.2). If these systems are counted once, the merging fractions are 56/99 (57^{+5}_{-6}%) and 28/99 ($28\% \pm 5\%$) for all merger candidates and major mergers, respectively. We stress that the possible companions are not spectroscopically confirmed and some of them may be foreground or background galaxies.

We also study the F770W-band morphology of the 38/258 AS2COSMOS sources in the coverage of both NIRCam and MIRI imaging (Figure 13 in Appendix A), which is considered to better trace obscured AGN activity. We find that AS2COS0019.1 and AS2COS0048.1 have pointlike morphology in the MIRI/F770W band. These sources are confirmed to host AGNs by SED analysis, and their mid-infrared emission is expected to be dominated by the AGN component. Thus, the pointlike morphology in the MIRI/F770W band is consistent with AGN emission, as predicted by the SED analysis.

4. Results and Discussion

In this section, we discuss the physical properties of the X-ray-detected and SED AGN SMGs, including a comparison of their far-infrared and X-ray luminosities, their SED-derived host-galaxy properties, X-ray absorption, and X-ray versus bolometric luminosities of the AGNs and their SFRs (Sections 4.1–4.5), before ending on a discussion of the population statistics of AGNs in SMGs and their connection to dynamical interactions as indicated by JWST imaging. The sample of the X-ray and SED AGNs is summarized in Table 1. The complete table, including infrared luminosity, dust luminosity, dust mass, dust temperature, and color excess of dust attenuation for stellar emission, is provided as supplemental material. The SEDs and the best-fit models of the SED AGNs are summarized in Appendix G. We also show the X-ray spectra and the line-of-sight hydrogen column densities of the 23 X-ray-detected SMGs in Appendix G.

4.1. Comparison of Far-infrared Luminosity and X-Ray Luminosity

Figure 7 compares the rest-frame far-infrared (40–120 μm) luminosities and the X-ray luminosities for the X-ray-detected AS2COSMOS sources. We also plot the empirical relation for local quasars (M. Elvis et al. 1994), AGN-classified SMGs, and starburst-classified SMGs (D. M. Alexander et al. 2005). We confirm that the X-ray-detected AS2COSMOS sources have more than 1 dex higher X-ray luminosities than those expected from their star formation activity ($L_X = 10^{-4} L_{\rm FIR}$). This suggests that the X-ray emission is dominated by AGNs, which verifies the assumption that the X-ray-detected AS2COSMOS sources host AGNs. Thus, we regard these sources as "X-ray AGNs" in the following sections. Note that the X-ray to far-infrared luminosity correlation in galaxies without AGNs has also been studied by a recent Chandra study in the Great Observatories All-Sky LIRG survey (N. Torres-Albà et al. 2018). According to their relation, even galaxies with $L_{\rm FIR} = 10^{46}$ erg s^{-1} ($\sim 10^{12.4}$ $L_\odot$) cannot be brighter than $L_X = 10^{42}$ erg s^{-1}. Thus, we may conservatively say that the X-ray emission in our X-ray AGN sample is dominated by the AGN activities. The X-ray AGN sample exhibits about a

---

[20] The strongly lensed system (AS2COS0005.1 and AS2COS0005.2) is excluded.

Table 1
Physical Properties of X-Ray AGNs and SED AGNs in the AS2COSMOS SMG Sample

ID	R.A. (deg)	Decl. (deg)	z	$\mathrm{Log_{10}}M_*$ ($M_\odot$)	$\mathrm{Log_{10}SFR}$ ($M_\odot\,\mathrm{yr^{-1}}$)	f_{AGN}	$\Delta\mathrm{BIC}$	$\mathrm{Log_{10}}L_{\mathrm{AGN,\,bol}}^{\mathrm{SED}}$ (erg s^{-1})	$\mathrm{Log_{10}}N_{\mathrm{H,X}}^{\mathrm{LOS}}$ (cm^{-2})	$\mathrm{Log_{10}}L_{\mathrm{2-10\,keV}}$ (erg s^{-1})
(1)	(2)	(3)	(4)	(5)	(6)	(7)	(8)	(9)	(10)	(11)
Only X-Ray AGNs										
AS2COS0014.1	150.42100	2.06802	2.921	11.50 ± 0.13	2.89 ± 0.05	$\cdots$	-3.6	< 46.37	$23.4^{+0.3}_{-0.4}$	$44.06^{+0.25}_{-0.26}$
AS2COS0031.1	149.84586	2.86042	3.643	11.24 ± 0.12	3.20 ± 0.05	$\cdots$	-3.0	< 46.24	$22.9^{+0.5}_{\mathrm{lim}}$	$44.21^{+0.22}_{-0.23}$
AS2COS0036.1	150.10616	2.01437	1.61 ± 0.11	11.69 ± 0.07	2.43 ± 0.24	$\cdots$	-0.7	< 46.39	$22.5^{+0.3}_{-0.4}$	$43.63^{+0.14}_{-0.14}$
AS2COS0055.2	150.32147	1.71421	0.69 ± 0.03	11.16 ± 0.05	0.54 ± 0.31	$\cdots$	-12.2	< 44.45	$21.9^{+0.2}_{-0.4}$	$42.95^{+0.10}_{-0.10}$
AS2COS0066.1	149.94410	1.95418	3.247	11.07 ± 0.15	2.84 ± 0.08	$\cdots$	-10.6	< 46.08	$22.8^{+0.5}_{\mathrm{lim}}$	$43.87^{+0.25}_{-0.26}$
AS2COS0068.1	150.14291	2.05061	2.433	11.39 ± 0.02	2.51 ± 0.03	$\cdots$	-1.1	< 46.37	$23.5^{+0.1}_{-0.2}$	$44.61^{+0.14}_{-0.13}$
AS2COS0069.1	149.77102	2.36576	3.618	10.28 ± 0.05	3.27 ± 0.02	$\cdots$	-2.0	< 46.40	$23.8^{+0.3}_{-0.3}$	$44.54^{+0.30}_{-0.30}$
AS2COS0076.2	150.38353	2.07446	4.47 ± 1.20	10.30 ± 0.37	3.26 ± 0.37	$\cdots$	-4.1	< 45.42	$23.8^{+0.4}_{-0.4}$	$44.74^{+0.37}_{-0.32}$
AS2COS0095.2	150.12596	2.69636	1.66 ± 0.12	11.37 ± 0.07	2.12 ± 0.20	$\cdots$	-6.2	< 46.30	$22.2^{+0.4}_{-1.3}$	$43.69^{+0.11}_{-0.11}$
AS2COS0133.1	149.99979	2.10924	3.59 ± 0.23	10.46 ± 0.31	3.07 ± 0.16	$\cdots$	6.1	< 45.72	$23.7^{+0.2}_{-0.2}$	$44.65^{+0.19}_{-0.20}$
AS2COS0153.2	149.88157	2.31819	1.616	10.84 ± 0.18	2.77 ± 0.08	$\cdots$	-5.1	< 45.96	$22.4^{+0.4}_{-0.4}$	$43.74^{+0.11}_{-0.11}$
AS2COS0220.1	150.00780	1.68614	4.00 ± 0.57	10.94 ± 0.18	3.03 ± 0.18	$\cdots$	-12.4	< 46.34	$23.8^{+0.3}_{-0.3}$	$44.70^{+0.27}_{-0.25}$
AS2COS0246.2	150.50454	2.72503	3.18 ± 0.06	10.35 ± 0.04	2.66 ± 0.03	$\cdots$	3.2	< 45.77	$22.7^{+0.4}_{\mathrm{lim}}$	$44.28^{+0.13}_{-0.13}$
AS2COS0272.1	150.31664	1.60374	3.65 ± 0.67	11.29 ± 0.21	3.22 ± 0.23	$\cdots$	-9.0	< 48.01	$22.8^{+0.4}_{\mathrm{lim}}$	$44.42^{+0.17}_{-0.17}$
AS2COS0275.2	149.95169	1.74405	1.632	10.85 ± 0.12	2.92 ± 0.04	$\cdots$	-1.3	< 46.25	$22.6^{+0.3}_{-0.7}$	$43.43^{+0.19}_{-0.20}$
AS2COS0353.1	149.51390	2.04452	3.13 ± 0.26	9.54 ± 0.20	2.45 ± 0.14	$\cdots$	-8.3	< 46.41	$23.9^{+0.3}_{-0.3}$	$44.51^{+0.32}_{-0.35}$
X-ray AGNs $\cap$ SED AGNs										
AS2COS0019.1	150.15840	2.13955	1.825	10.37 ± 0.28	3.15 ± 0.08	0.22 ± 0.04	74.9	45.99 ± 0.04	$22.4^{+0.1}_{-0.2}$	$44.42^{+0.05}_{-0.05}$
AS2COS0028.2	149.99795	2.57821	2.15 ± 0.10	10.14 ± 0.25	2.87 ± 0.29	0.29 ± 0.17	19.0	46.42 ± 0.03	$23.9^{+0.2}_{-0.2}$	$44.48^{+0.29}_{-0.27}$
AS2COS0048.1	150.28853	2.38193	1.581	11.62 ± 0.06	1.91 ± 0.06	0.57 ± 0.05	11.0	46.25 ± 0.08	$22.6^{+0.2}_{-0.2}$	$43.76^{+0.10}_{-0.09}$
AS2COS0116.2	150.49037	1.74637	2.38 ± 0.17	10.85 ± 0.23	2.49 ± 0.14	0.61 ± 0.04	100.3	46.75 ± 0.05	$23.5^{+0.1}_{-0.1}$	$44.73^{+0.11}_{-0.10}$
AS2COS0175.1	150.73578	2.19958	3.509	12.40 ± 0.84	1.78 ± 1.34	0.30 ± 0.02	151.3	46.56 ± 0.02	$20.0^{+2.6}_{\mathrm{lim}}$	$44.59^{+0.09}_{-0.07}$
AS2COS0230.1	149.61511	1.78955	1.84 ± 0.23	10.56 ± 0.30	2.71 ± 0.17	0.10 ± 0.01	14.8	45.22 ± 0.08	$22.2^{+0.6}_{\mathrm{lim}}$	$43.72^{+0.15}_{-0.15}$
AS2COS0308.1	150.60879	2.76970	3.026	11.01 ± 0.06	3.22 ± 0.02	0.41 ± 0.04	33.3	46.77 ± 0.11	$22.6^{+0.3}_{-0.6}$	$44.93^{+0.06}_{-0.06}$
Only SED AGNs										
AS2COS0001.1	150.03350	2.43675	4.625	10.33 ± 0.22	3.19 ± 0.12	0.56 ± 0.13	57.2	46.96 ± 0.16	$\cdots$	< 44.89
AS2COS0008.1	150.70497	2.54874	3.581	11.96 ± 0.07	2.27 ± 0.09	0.38 ± 0.05	15.8	46.38 ± 0.09	$\cdots$	< 44.93
AS2COS0024.1	150.13265	2.21184	2.176	11.25 ± 0.09	2.54 ± 0.14	0.55 ± 0.09	37.9	46.46 ± 0.07	$\cdots$	< 44.47
AS2COS0025.1	150.16352	2.37252	2.086	10.51 ± 0.12	2.70 ± 0.05	0.49 ± 0.03	13.3	46.42 ± 0.04	$\cdots$	< 44.41
AS2COS0054.1	149.69140	2.72481	3.176	10.86 ± 0.23	2.88 ± 0.15	0.55 ± 0.13	24.3	46.62 ± 0.08	$\cdots$	< 44.66
AS2COS0076.1	150.38388	2.07448	3.08 ± 0.30	10.04 ± 0.38	2.49 ± 0.17	0.65 ± 0.09	31.3	46.39 ± 0.03	$\cdots$	< 45.07
AS2COS0078.3	150.44575	2.41303	2.75 ± 0.18	10.93 ± 0.13	2.35 ± 0.16	0.46 ± 0.14	13.8	46.19 ± 0.10	$\cdots$	< 45.04
AS2COS0084.1	149.58108	2.25228	3.600	9.69 ± 0.12	2.64 ± 0.06	0.40 ± 0.08	21.6	46.08 ± 0.10	$\cdots$	< 44.90
AS2COS0099.1	149.92558	1.77732	1.60 ± 0.20	10.18 ± 0.88	2.04 ± 1.62	0.88 ± 0.04	27.2	46.89 ± 0.03	$\cdots$	< 44.30
AS2COS0108.2	150.09505	1.86019	3.85 ± 0.80	9.23 ± 0.23	2.16 ± 0.19	0.89 ± 0.03	14.9	46.71 ± 0.07	$\cdots$	< 44.81
AS2COS0123.1	149.59827	2.20781	4.84 ± 0.25	9.58 ± 0.14	2.53 ± 0.08	0.90 ± 0.02	16.4	47.03 ± 0.06	$\cdots$	< 45.00
AS2COS0139.1	149.58247	2.60280	3.292	10.43 ± 0.05	3.42 ± 0.02	0.49 ± 0.03	131.2	47.31 ± 0.03	$\cdots$	< 44.75
AS2COS0189.1	149.49363	2.28020	2.79 ± 0.61	9.78 ± 0.33	2.62 ± 0.28	0.35 ± 0.22	30.1	46.15 ± 0.73	$\cdots$	< 44.76
AS2COS0231.1	149.78372	2.81792	1.97 ± 0.14	11.21 ± 0.14	2.31 ± 0.14	0.69 ± 0.08	44.8	46.47 ± 0.07	$\cdots$	< 44.48

Table 1
(Continued)

ID	R.A. (deg)	Decl. (deg)	z	$\mathrm{Log}_{10}M_*$ ($M_\odot$)	$\mathrm{Log}_{10}\mathrm{SFR}$ ($M_\odot\,\mathrm{yr}^{-1}$)	f_AGN	$\Delta\mathrm{BIC}$	$\mathrm{Log}_{10}L_\mathrm{AGN,\,bol}^\mathrm{SED}$ (erg s^{-1})	$\mathrm{Log}_{10}N_\mathrm{H,X}^\mathrm{LOS}$ (cm^{-2})	$\mathrm{Log}_{10}L_\mathrm{2-10\ keV}$ (erg s^{-1})
(1)	(2)	(3)	(4)	(5)	(6)	(7)	(8)	(9)	(10)	(11)
AS2COS0261.1	149.64308	1.91751	1.83 ± 0.16	10.93 ± 0.10	2.17 ± 0.11	0.63 ± 0.05	12.6	46.16 ± 0.06	$\cdots$	< 44.59
AS2COS0330.3	150.76551	1.73478	3.74 ± 0.09	10.34 ± 0.22	2.74 ± 0.15	0.70 ± 0.07	27.4	46.66 ± 0.06	$\cdots$	< 45.05
AS2COS0362.1	149.69350	1.72286	3.79 ± 0.12	10.81 ± 0.09	2.50 ± 0.12	0.69 ± 0.07	31.6	46.57 ± 0.03	$\cdots$	< 44.89

Note. Columns (1), (2), and (3): ALMA source ID and positions (same as J. M. Simpson et al. 2020). Column (4): redshift (three decimal digits are for spectroscopic redshifts and two are for photometric redshifts). Column (5): stellar mass. Column (6): SFR. Column (7): luminosity fraction of AGNs in total infrared luminosity (f_AGN). Column (8): change in BIC by the addition of an AGN component in the SED modeling. Column (9): bolometric AGN luminosity estimated by SED modeling (the uncertainties listed in this table are converted from those calculated in the linear space). Column (10): line-of-sight hydrogen column density (parameters that reach the model limits are indicated by "lim"). Column (11): X-ray luminosity (the values in parentheses show the X-ray luminosities assuming Compton-thick absorption; $N_\mathrm{H,X}^\mathrm{LOS} = 9.8 \times 10^{24}$ cm^{-2}). The redshift uncertainties are not considered for the calculation of $L_\mathrm{AGN,\,bol}^\mathrm{SED}$, $N_\mathrm{H,X}^\mathrm{LOS}$, and $L_\mathrm{2-10\ keV}$. The upper bounds correspond to the 99.73% confidence (3σ). Note that the reduced χ^2 values of these AGNs are lower than 5 (well fitted).
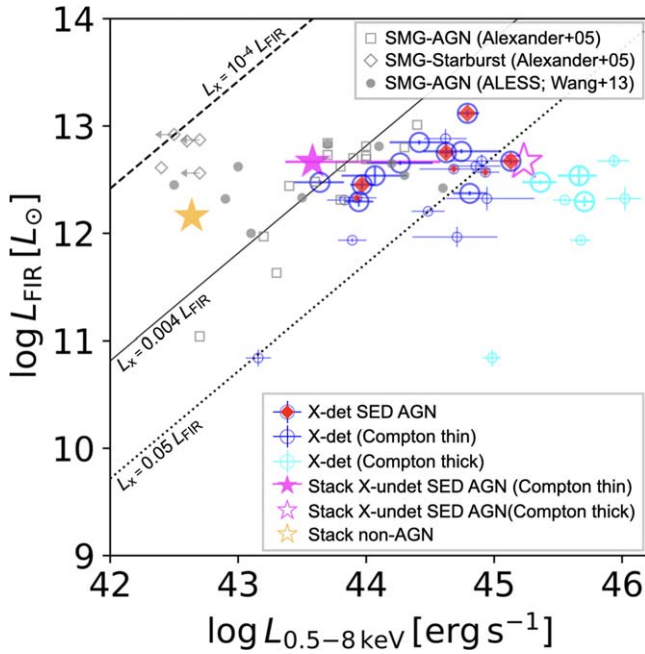
Figure 7. Comparison between far-infrared luminosity (rest-frame 40–120 μm) and X-ray (rest-frame 0.5–8 keV) luminosity for X-ray-detected (X-det) SMGs. For the AS2COSMOS sources, we apply a factor of $1/1.91$ to convert total infrared luminosity to far-infrared luminosity (B. Magnelli et al. 2012). In addition, we convert the rest-frame 2–10 keV luminosity to rest-frame 0.5–8 keV luminosity assuming an intrinsic power-law spectrum with a photon index of 1.9. The stacked values of X-ray-undetected (X-undet) SED AGNs and non-AGNs are also plotted. The solid and dashed lines show the empirical relations of AGN-classified SMGs and starburst-classified SMGs, respectively (D. M. Alexander et al. 2005). The dotted line shows the empirical relation of local quasars (M. Elvis et al. 1994). The large symbols show the spec-z sample, while the smaller ones show the photo-z sample. The redshift uncertainties are not considered in these plots. The X-ray-detected AS2COSMOS sources have more than 1 dex higher X-ray luminosities than those expected from the empirical relation of starburst-classified SMGs, suggesting that the X-ray emission is dominated by AGNs.

median of 6 times higher X-ray luminosities than the empirical relation of AGN-classified SMGs ($L_X = 0.004L_{FIR}$), assuming Compton-thin absorption. This can be attributed to the selection using the relatively shallow X-ray observations in the COSMOS field, as compared with the deeper Chandra observations employed in D. M. Alexander et al. (2005).

Regarding the X-ray stacking analysis, we plot in Figure 7 the median far-infrared luminosities and the stacked X-ray luminosities for the X-ray-undetected SED AGNs. We find that the stacked values are consistent with the empirical relation of AGN-classified SMGs assuming Compton-thin absorption. This implies that the X-ray-undetected SED AGNs are probably the same population as the AGN-classified SMGs reported in the previous studies using deeper X-ray observations (D. M. Alexander et al. 2005; S. X. Wang et al. 2013). On the other hand, if we consider the Compton-thick case, the stacked values align with the empirical relation of local quasars ($L_X = 0.05L_{FIR}$). To distinguish between these two possibilities, deeper hard X-ray observations above rest-frame 10 keV are needed. Moreover, we plot the median far-infrared luminosities and the stacked X-ray luminosities of the non-AGNs. We find that the stacked X-ray luminosity is $\sim$0.7 dex higher than that expected from their star formation activity. This supports the prediction in Section 3.2.3 that there remain obscured AGNs that are neither detected in X-ray nor identified

as SED AGNs. Thus, we also calculate the upper bound of the AGN luminosity in the non-AGN sample from the integrated count rate derived from our stacking analysis, which is used in Section 4.5. Here we assume the same X-ray spectral model as in Section 3.2.2 placed at the median redshift of $z = 2.45$, and the line-of-sight hydrogen column density is fixed to $N_{H,X}^{LOS} \sim 10^{23.2}$ cm^{-2} as predicted by the stacking analysis (Section 3.2.3).

4.2. X-Ray Absorption by Host-galaxy Gas

If we make assumptions about the distribution of dust and gas-to-dust ratio, we can estimate the line-of-sight hydrogen column densities of the host-galaxy dust based on the dust masses and the sizes of the dust-emitting regions. We assume that the half-mass of galaxy dust is uniformly distributed within a sphere with a half-light radius centered at the SMBH. The H_2-to-dust mass ratio is fixed to 90 (A. M. Swinbank et al. 2014). Based on these assumptions across the whole sample, the median hydrogen column density in the molecular phase is estimated as $N_{H,dust}^{mol} = 8.7_{-0.3}^{+0.9} \times 10^{23}$ cm^{-2}, which is consistent with the previous study of the bright subsample of AS2UDS ($N_{H,dust}^{mol} = 9.8_{-0.7}^{+1.4} \times 10^{23}$ cm^{-2}; J. M. Simpson et al. 2017). Then, we convert the hydrogen column density in the molecular phase to total hydrogen column density by applying a factor of 2.5 following C. Andonie et al. (2024), which is based on theoretical models by C. D. P. Lagos et al. (2011) and J. Fu et al. (2012). Finally, we obtain the median hydrogen column density of $N_{H,dust} = 1.4_{-0.6}^{+0.5} \times 10^{24}$ cm^{-2}, $N_{H,dust} = 3.0_{-1.1}^{+0.7} \times 10^{24}$ cm^{-2}, and $N_{H,dust} = 2.2_{-0.1}^{+0.2} \times 10^{24}$ cm^{-2} for the X-ray AGNs, the SED AGNs, and the rest of the AS2COSMOS sources, respectively. These values are slightly higher than the previous report on the average ISM column density of 24 submillimeter-infrared quasars at $z \sim 1–3$ in the COSMOS field: $\langle N_{H,ISM} \rangle_{submm-IRquasars} = (0.8 \pm 0.1) \times 10^{24}$ cm^{-2} (C. Andonie et al. 2024). Given the tight correlation between dust mass and 870 μm flux density (U. Dudzevičiūtė et al. 2020), this may be attributed to the bright submillimeter selection of our sample.

Figure 8(a) compares the line-of-sight hydrogen column density measured by X-ray spectral analysis ($N_{H,X}^{LOS}$) with that estimated by the dust properties ($N_{H,dust}^{mol}$). In the majority of cases (18/21), the line-of-sight hydrogen column density estimated from the dust properties is significantly larger than the X-ray measurements in the Compton-thin cases. This suggests that the host-galaxy clouds have nonspherical geometry and/or have complex (e.g., clumpy) distributions. We may also consider the possibility that the X-ray absorption of those sources is dominated by the opacity in the host galaxy rather than the torus. Moreover, this result might suggest that many of the X-ray AGNs are Compton thick and the line-of-sight hydrogen column densities are not properly constrained by the X-ray spectral analysis. Figure 8(b) shows the histogram of the line-of-sight hydrogen column density estimated from the dust properties. We find that the SED AGNs have tentatively $\sim$0.3 dex higher column densities than the X-ray AGNs. The median value of the SED AGNs is $N_{H,dust}^{mol} = 1.2_{-0.4}^{+0.3} \times 10^{24}$ cm^{-2}, which is broadly equivalent to the threshold of Compton-thick absorption ($N_H = 1.7 \times 10^{24}$ cm^{-2}). Thus, this might suggest that in bright SMGs AGNs can be heavily obscured by the host galaxies, which makes them difficult to detect with X-ray observations.
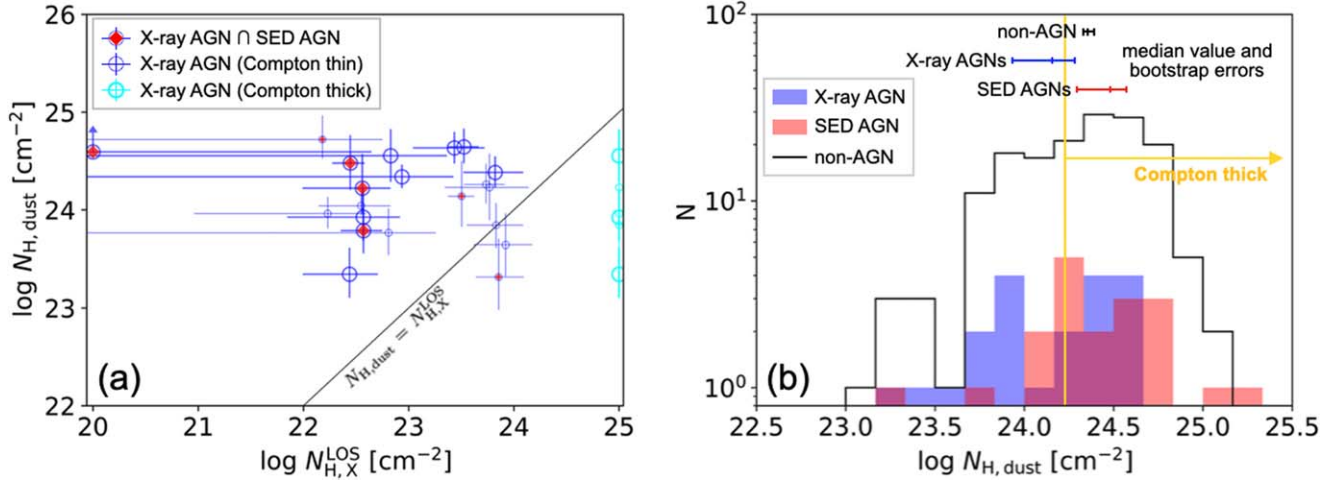
Figure 8. (a) Comparison of line-of-sight hydrogen column density measured by X-ray spectral analysis ($N_{\mathrm{H,X}}^{\mathrm{LOS}}$) with that estimated from the dust properties ($N_{\mathrm{H,dust}}$). AS2COS0055.2 and AS2COS246.2 are not plotted in this panel because they are too faint to derive reliable sizes. The large symbols show the spec-z sample, while the smaller ones show the photo-z sample. (b) Histogram of the line-of-sight hydrogen column density calculated from the dust properties for the X-ray AGNs, the SED AGNs, and the rest of the AS2COSMOS sources (non-AGNs). Only the sources whose sizes are well constrained are included in these histograms. The vertical solid line shows the threshold of Compton-thick absorption ($N_{\mathrm{H}} = 1.7 \times 10^{24}$ cm^{-2}). The redshift uncertainties are not considered when calculating the plotted values in these panels.

4.3. Comparison of Physical Properties between Samples

Figure 9 compares the stellar masses, SFRs, sSFRs, radio$-$IR correlation factors, and sizes of the dust-emitting regions of the X-ray AGNs, the SED AGNs, and the rest of the AS2COSMOS sources (non-AGNs). We find that the median SFR and stellar mass of the X-ray AGN sample ($\log \mathrm{SFR}[M_\odot \ \mathrm{yr}^{-1}] = 2.84_{-0.13}^{+0.05}$ and $\log M_*[M_\odot] = 10.94_{-0.09}^{+0.12}$) are about two times higher than those of the non-AGN sample ($\log \mathrm{SFR}[M_\odot \ \mathrm{yr}^{-1}] = 2.53_{-0.06}^{+0.02}$ and $\log M_*[M_\odot] = 10.62_{-0.09}^{+0.04}$), while the median SFR and stellar mass of the SED AGN sample ($\log \mathrm{SFR}[M_\odot \ \mathrm{yr}^{-1}] = 2.53_{-0.04}^{+0.10}$ and $\log M_*[M_\odot] = 10.53_{-0.16}^{+0.30}$) agree with those of the non-AGNs. This might be attributed to the X-ray selection bias of these sources. Since the X-ray observations in the COSMOS field are relatively shallow, the X-ray AGNs are biased to bright AGNs, which likely host higher-mass SMBHs. Hence, if we assume a positive correlation between stellar mass and SMBH mass (J. Kormendy & L. C. Ho 2013), the X-ray AGNs are expected to be hosted by massive galaxies, which may have a high SFR according to the scaling relation of SFR and stellar mass. This argument is supported by the similarity in the distributions of the sSFRs between the X-ray AGNs, SED AGNs, and non-AGNs (the median sSFRs of the X-ray AGN, SED AGN, and non-AGN samples are $-8.04_{-0.04}^{+0.12}$ yr^{-1}, $-7.83_{-0.31}^{+0.23}$ yr^{-1}, and $-7.99_{-0.03}^{+0.10}$ yr^{-1}, respectively). We also find that the radio–IR correlation factors and the dust continuum sizes do not significantly vary between the samples. This implies that the vast majority of the X-ray AGNs and the SED AGNs are radio-quiet and the properties of their host galaxy are similar to those of the non-AGNs.

4.4. X-Ray Luminosity versus Bolometric AGN Luminosity

Figure 10 compares the X-ray-to-bolometric correction factor ($\kappa_{2-10} = L_{\mathrm{AGN, bol}}/L_{2-10\,\mathrm{keV}}$) with the bolometric AGN luminosity for our AGN samples. We also plot the empirical relation of AGNs at $z < 3.5$ from F. Duras et al. (2020). We find that six out of the seven X-ray-detected SED AGNs show

good agreement with the empirical relation, while one source has about 1 dex higher X-ray luminosity than the empirical relation (AS2COS0048.1; $\kappa_{2-10} = 326$). We also find that all the X-ray AGNs are predicted to be Compton-thin AGNs, while the majority of the X-ray-undetected SED AGNs (14/17) appear to be nearly Compton thick ($N_{\mathrm{H,X}}^{\mathrm{LOS}} \gtrsim 10^{24}$ cm^{-2}), assuming that the empirical relation holds. This is consistent with the recent observation that a significant fraction of AGNs in local ultra/luminous infrared galaxies (U/LIRGs; $L_{\mathrm{IR}}/L_\odot > 10^{11}$) show Compton-thick absorption (16/35; C. Ricci et al. 2021). However, some studies have reported that AGNs in the local U/LIRGs are intrinsically X-ray weak ($\kappa_{2-10} = 100$–1000; S. H. Teng et al. 2014; S. Yamada et al. 2021). If this phenomenon is applicable to our samples, the X-ray-undetected SED AGNs do not have to be Compton thick. Note that the X-ray AGNs are not predicted to be intrinsically X-ray weak, based on the upper limits of the X-ray-to-bolometric correction factors.

Regarding the X-ray stacking analysis, we plot the average X-ray-to-bolometric correction factors and the median bolometric AGN luminosities for the X-ray-undetected SED AGNs. We find that, assuming the Compton-thin case, the inferred average X-ray-to-bolometric corrections for the X-ray-undetected SED AGNs are more than 1 dex higher than the empirical relation and higher than any X-ray-detected SED AGNs in our sample. This may indicate that the X-ray-undetected SED AGNs are either Compton thin and intrinsically X-ray weak or are Compton thick.

4.5. SFR versus Bolometric AGN Luminosity

Figure 11 compares the SFR with the bolometric AGN luminosity for the X-ray AGNs and SED AGNs. Here we use the bolometric AGN luminosity derived from the SED modeling for the SED AGNs. For X-ray AGNs, excluding X-ray AGNs that are also identified as SED AGNs, the bolometric AGN luminosities are converted from the X-ray luminosities using the calibration by F. Duras et al. (2020). Note that we use the X-ray luminosities calculated with the
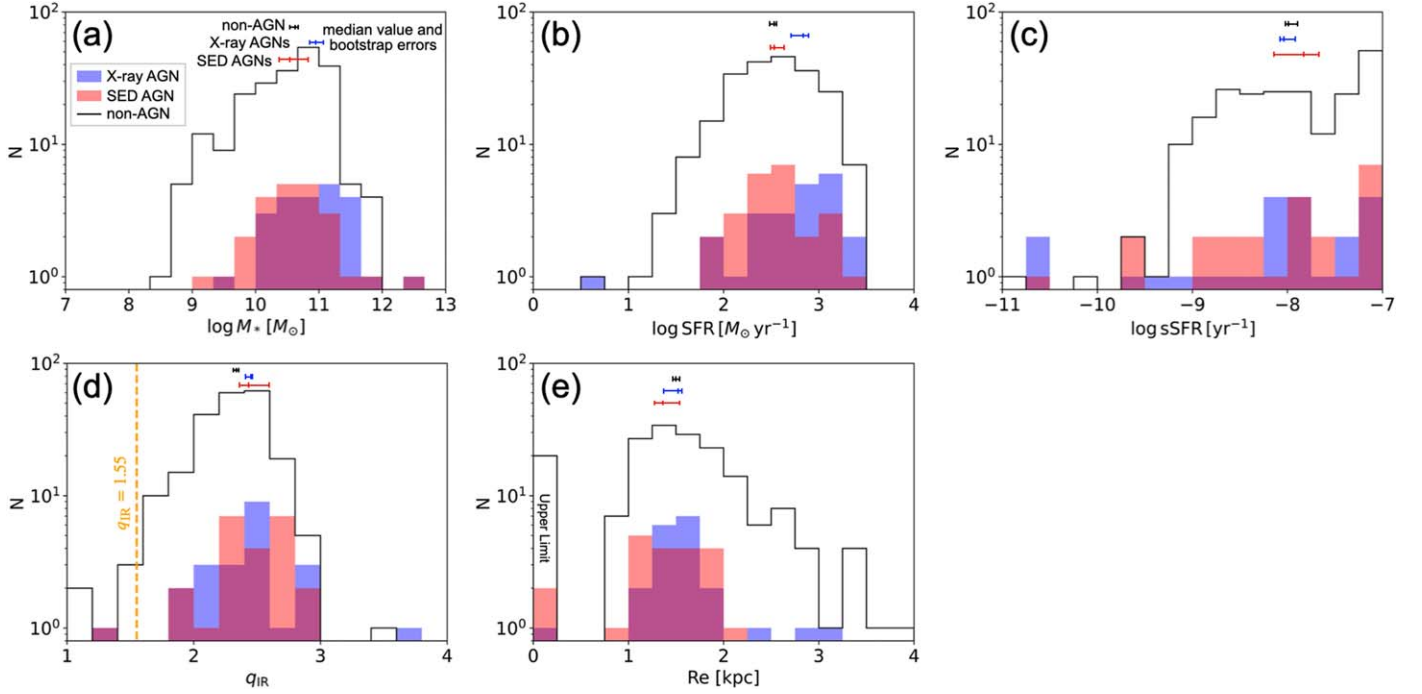
Figure 9. Histograms of (a) stellar masses, (b) SFRs, (c) sSFRs, (d) radio–IR correlation factors (q_{IR}), and (e) the dust continuum sizes (R_e) for the X-ray AGNs, the SED AGNs, and the rest of the AS2COSMOS sources (non-AGNs). In the histogram of R_e, the bins at $R_e = 0$ kpc show the number of sources whose dust sizes are only given as the upper confidence intervals. We confirm no significant difference between the samples, suggesting the similarity of their host galaxies, regardless of the presence of an X-ray or SED AGN.
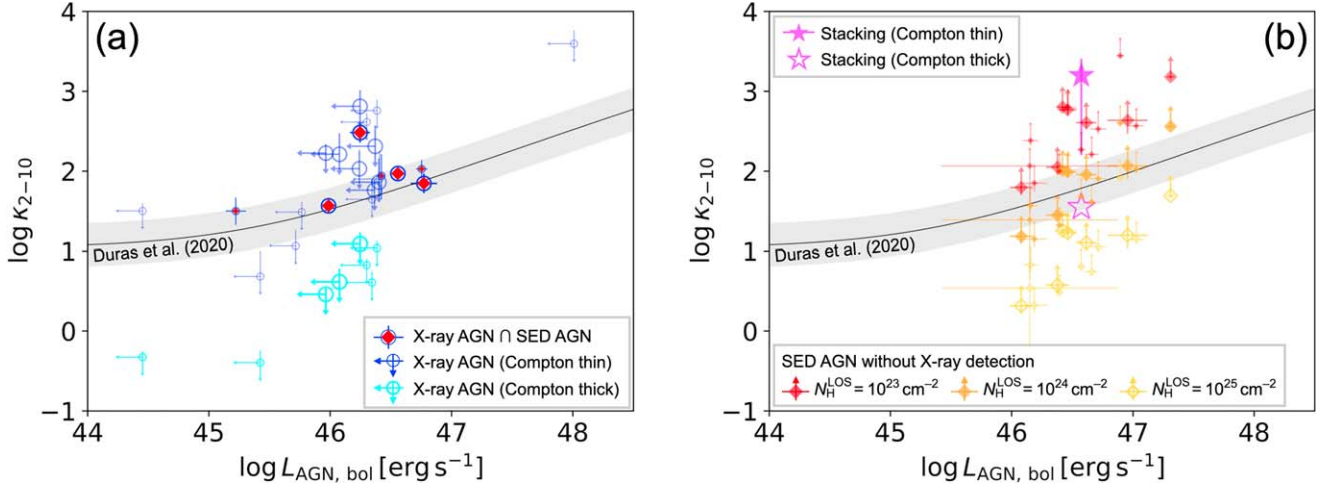
Figure 10. Comparison of X-ray-to-bolometric correction factor (κ_{2-10}) and bolometric AGN luminosity for (a) the X-ray AGNs and (b) the SED AGNs (the overlapped sources are plotted in panel (a)). The black solid line denotes the empirical relation at $z = 0$–4 (F. Duras et al. 2020). Symbols with arrows show the 3σ upper bound for each parameter. The redshift uncertainties are not considered when calculating the overall uncertainties of the plotted values. The large symbols show the spec-z sample, while the smaller ones show the photo-z sample. We find that the X-ray AGNs are predicted to be Compton-thin AGNs, while the majority of X-ray-undetected SED AGNs are nearly Compton-thick AGNs, if the empirical relation holds.

Compton-thin assumption based on the discussion in Section 4.4. We also plot the median SFR and the upper bound of the bolometric AGN luminosity for the non-AGN sample calculated from the X-ray stacking (Section 4.1), where the calibration by F. Duras et al. (2020) is adopted to convert the X-ray luminosity upper bound to the bolometric AGN luminosity upper bound. For comparison, we plot the "simultaneous galaxy–SMBH evolution" line for the coevolution of SMBHs and the host galaxies. Assuming that SMBHs and the host galaxies coevolve simultaneously across cosmic time, the relative ratio of star formation and AGN activity is

expected to track this relationship:

$$\begin{aligned}\mathrm{SFR} \times (1 - R) &= A \times \dot{M}_{BH}\\ &= L_{\mathrm{AGN, bol}} \times (1 - \eta)/\eta c^2,\end{aligned} \quad (5)$$

where R is the return function (the fraction of stellar masses that are ejected back to the interstellar medium), A is the mass ratio of stars to SMBHs, η is the accretion efficiency, and c is the speed of light. We assume $R = 0.41$ (Chabrier IMF) and $\eta = 0.05$. For A, we calculate in two settings: $A = 200$ and $A = 400$. The former value is the typical mass ratio of stars in
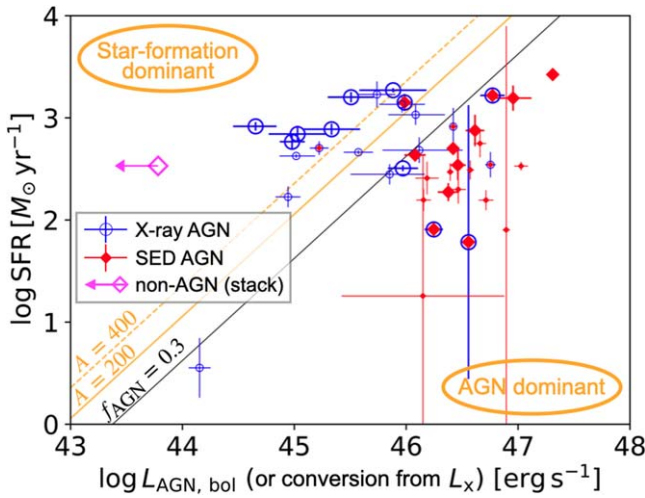
Figure 11. Comparison of SFR and bolometric AGN luminosity for the X-ray AGNs and the SED AGNs. The orange solid and dashed lines show the "simultaneous evolution" with $A = 200$ (bulge only) and $A = 400$ (bulge +disk), respectively. The black solid line shows the detection limit of the type 2 SED AGNs (see Section 3.1.5). The large symbols show the spec-z sample, while the smaller ones show the photo-z sample. We find that the SED AGNs are distributed in the AGN-dominant region, suggesting that in such a phase AGNs can be nearly Compton thick and missed in X-ray.

bulge components to SMBHs in the local universe (J. Kormendy & L. C. Ho 2013), while the latter value includes the disk components (see Section 4.4 in Y. Ueda et al. 2018). We find that the SED AGNs are distributed in the AGN-dominant phase, where SMBHs grow faster than the host galaxies, while the X-ray AGNs are almost distributed around the simultaneous evolution lines. The bias of SED AGNs to higher AGN luminosity can be explained by the selection effect discussed in Section 3.1.5. We can potentially interpret these results within the merger-driven evolutionary scenario: on the basis of this scenario, galaxy mergers first trigger star formation activity and later evoke AGN activity after the gas has had time to reach the nuclear region (e.g., via stellar winds, via supernovae, or through gravitational torques). Within this scenario, the SED AGNs would correspond to the transition phase, where merging has reached the nuclear regions and the AGN activity has been enhanced, but the star formation is not yet quenched. Hence, we might say that in such phases AGNs are likely to be heavily obscured by dust or have unusually suppressed X-ray emissions, which makes them difficult to detect with X-ray observations. We note that the selection of the AGNs by SED modeling strongly depends on the quality of the multi-wavelength photometry and the assumptions of models. Thus, these results should be verified by other methods like future sensitive observations with the Advanced Telescope for High Energy Astrophysics (Athena; K. Nandra et al. 2013).

4.6. Population Statistics

4.6.1. AGN Number Fraction

The depths of the X-ray observations in the COSMOS field are only moderate ($\sim$160 ks pixel^{-1}). Thus, the X-ray AGNs in the AS2COSMOS sample are not complete even for X-ray-bright sources above luminosities of $L_X = 10^{43}$ erg s^{-1} cm^{-2}. The SED AGNs are also incomplete owing to the selection

shown in Section 3.1.5. Hence, the AGN number fraction in our sample provides a lower limit for bright SMGs. In this study, the AGN number fraction in the AS2COSMOS sample is estimated as $16^{+3}_{-2}\%$ for all AGNs (SED AGNs and X-ray AGNs) and $9\% \pm 2\%$ for only X-ray AGNs. The number fraction of X-ray AGNs in our sample is therefore consistent with that in the AS2UDS sample ($8\% \pm 2\%$; S. M. Stach et al. 2019), where the depths of the X-ray observations used in that work are more comparable to those in the COSMOS field (X-UDS; 200–600 ks with Chandra; D. D. Kocevski et al. 2018).

To identify trends in AGN fraction with the SMG population, we separate the sample into four bins based on the redshifts and 870 μm flux densities. Since our sample is only complete for SMGs brighter than $S_{850\,\mu m} = 6.2$ mJy, we separate the sample at $S_{870\,\mu m} = 6.2$ mJy. We also separate the sample at $z = 3$ because the selection of AGNs by SED modeling is more reliable at low redshift ($z < 3$; Section 3.1.3).

In the brighter SMG samples, the AGN number fraction (SED AGNs and X-ray AGNs) is about two times higher at high redshift ($24^{+8}_{-6}\%$) than at low redshift ($13^{+5}_{-4}\%$), which is also confirmed for X-ray AGNs ($10^{+6}_{-4}\%$ and $6^{+4}_{-2}\%$, respectively). This might suggest that the SMBH growth is more intense in high-redshift SMGs. However, we stress that the evidence for high-redshift SED AGNs ($z > 3$) is fairly limited and that care should be taken with this issue. For low-redshift samples, the SED AGN number fraction is higher in the brighter SMGs ($7^{+4}_{-3}\%$) than in the fainter SMGs ($1^{+2}_{-1}\%$), while the X-ray AGN number fractions are consistent within their confidence intervals ($6^{+4}_{-2}\%$ and $8^{+4}_{-3}\%$, respectively). This might suggest that, in bright SMGs, AGNs tend to be heavily obscured or have unusually weak X-ray emission. As the 870 μm flux density is tightly correlated with the dust mass of a galaxy (U. Dudzevičiūtė et al. 2020), this trend might be attributed to the dust obscuration by the host galaxies (Section 4.2). Nevertheless, we need to be cautious about the selection bias due to the quality of multiwavelength photometry. Brighter SMGs are more likely to have higher S/N in the mid- to far-infrared photometry, which can highlight the imperfection of the host-galaxy models and cause the misidentification of SED AGNs. On the other hand, in fainter SMGs, the S/N in the mid- to far-infrared photometry is expected to be lower, which can miss the presence of SED AGNs.

4.6.2. Merger Fraction

The connection between galaxy mergers and AGN/host-galaxy properties is an important but still unresolved issue. In the low-redshift universe ($z \lesssim 1$), several observational studies have shown that galaxies in mergers are more likely to host AGNs than isolated galaxies (e.g., A. D. Goulding et al. 2018; F. Gao et al. 2020). Theoretical investigations predict that the fraction of merger-induced starbursts in SMGs increases with submillimeter flux density (C. C. Hayward et al. 2013), although other theoretical work investigating the dependence of merger fraction on the stellar mass found that the merger fraction in SMGs is similar to the general galaxy population, suggesting that mergers are not the sole driver of the enhanced star formation in SMGs (S. McAlpine et al. 2019). To address this issue in our study, we examine the merger fraction of the AS2COSMOS sources as functions of stellar mass ($M_* > 10^{11}\,M_\odot$ or $M_* < 10^{11}\,M_\odot$) and AGN activity (AGN or non-AGN).
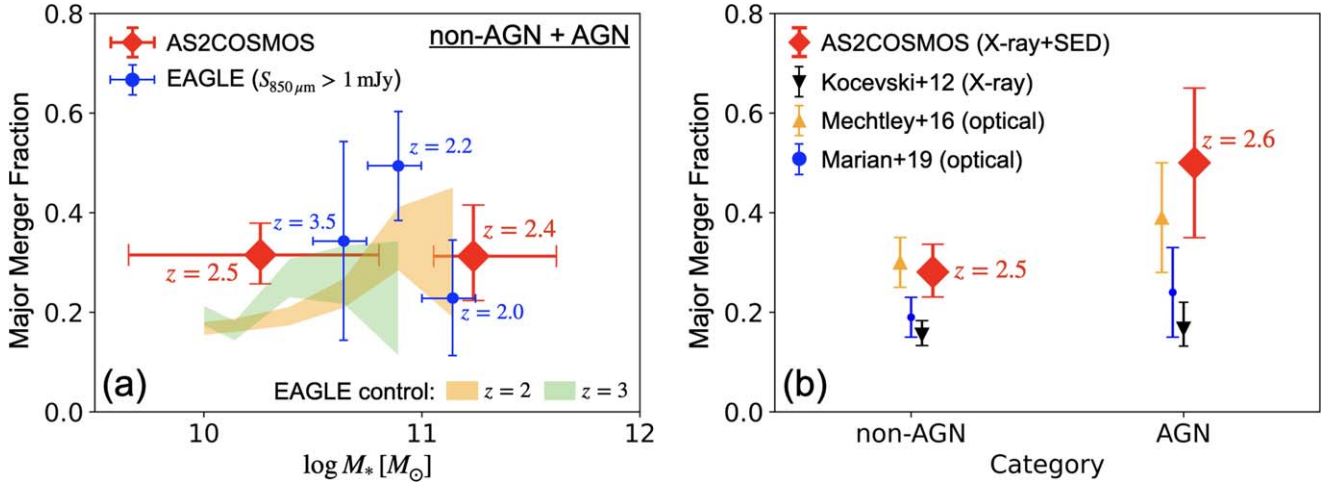
Figure 12. (a) Comparison of the major merger fraction in the AS2COSMOS sample with the theoretical prediction from EAGLE (S. McAlpine et al. 2019). The errors on M_* of the AS2COSMOS sample indicate the 16%–84% intervals of each stellar mass bin. (b) Dependencies of the major merger fraction as a function of AGN activity. The X-ray- and optical-selected AGNs at $z \sim 2$ are also plotted (D. D. Kocevski et al. 2012; M. Mechtley et al. 2016; V. Marian et al. 2019). Each data point is annotated with the median redshift of the galaxies in that bin. We find that major mergers may play a key role in triggering AGN activity in bright SMGs.

Figure 12(a) shows the dependence of major merger fractions on stellar masses. We also plot the theoretical prediction using the EAGLE simulation by S. McAlpine et al. (2019). We find no significant difference between the massive and less massive subsets of SMGs ($31^{+10}_{-9}\%$ and $32\% \pm 6\%$, respectively), and the major merger fractions of the two subsets are consistent with the EAGLE simulation. Figure 12(b) shows the dependence of major merger fractions on AGN activity. For comparison, we plot the major merger fractions in X-ray-selected AGNs (D. D. Kocevski et al. 2012) and optical-selected AGNs (M. Mechtley et al. 2016 and V. Marian et al. 2019) at $z \sim 2$ (see also C. Villforth 2023 for the summary of these studies). Notably, the major merger fraction in the AS2COSMOS non-AGN sample ($28^{+6}_{-5}\%$) is consistent with those of the general population at $z \sim 2$. However, we find that the major merger fraction in the AS2COSMOS AGN sample ($50\% \pm 15\%$) is potentially twice as high as that in the non-AGN sample, which is more significant than the enhancement reported for the general AGN samples at $z \sim 2$, although the uncertainties are large. These results suggest that major mergers are not necessarily required for the enhanced star formation in SMGs, as predicted by the EAGLE simulation, but may play a key role in triggering AGN activity in bright SMGs. We caution that there still remain large statistical uncertainties and that further studies with large samples are needed. For example, dependency of major merger fraction on AGN luminosity cannot be confirmed in this study but should be investigated in future studies with larger samples. In addition, the selection of AGNs by SED analysis strongly depends on the model assumptions. If we adopt the J. L. Donley et al. (2012) criteria for the selection of SED AGNs, the major merger fraction in the AGN sample is $43^{+13}_{-12}\%$, which is still almost consistent with the major merger fraction in our AGN sample. The slight difference might originate from the galaxy contamination in the J. L. Donley et al. (2012) selection. We also note that the stellar masses of most of the companions are not measured in this study, but it may not affect the main conclusion of this study.

5. Summary

We performed multicomponent SED modeling and X-ray spectral analysis for the sample of bright SMGs from the AS2COSMOS survey. The sample consists of 260 SMGs with $S_{870\,\mu m} = 0.7$–19.2 mJy, which is effectively complete for SMGs with 850 μm flux densities $S_{850\,\mu m} \geqslant 6.2$ mJy in the S2COSMOS catalog. Our main results are listed below:

1. Using an SED fitting methodology, we identified 24 AGN candidates (SED AGNs). Supplemented by 23 X-ray-detected AGNs (X-ray AGNs), we construct a sample of 40 AGN candidates, of which seven sources overlap between the two subsets.

2. The X-ray AGNs have a median of 6 times higher X-ray luminosities than the empirical relation between the X-ray luminosity and far-infrared luminosity for AGN-classified SMGs, assuming Compton-thin absorption. This can be attributed to the selection from the relatively shallow X-ray observations in the COSMOS field. An X-ray stacking analysis shows that the stacked luminosities of X-ray-undetected SED AGNs show good agreement with the empirical relation of the AGN-classified SMGs with the assumption of Compton-thin absorption. This indicates that the X-ray-undetected SED AGNs are likely to be the same population as the AGN-classified SMGs detected in deeper X-ray studies.

3. From the dust masses and the sizes of the dust-emitting region, the median hydrogen column densities are calculated as $N_{\rm H,dust} = 1.4^{+0.5}_{-0.6} \times 10^{24}$ cm^{-2}, $N_{\rm H,dust} = 3.0^{+0.7}_{-1.1} \times 10^{24}$ cm^{-2}, and $N_{\rm H,dust} = 2.2^{+0.2}_{-0.1} \times 10^{24}$ cm^{-2} for the X-ray AGNs, the SED AGNs, and the rest of the AS2COSMOS sources. The SED AGNs have about two times higher column densities than the X-ray AGNs. This may suggest that the SED AGNs are heavily obscured by the host-galaxy dust, which makes them difficult to detect with X-ray observations.

4. Among the seven X-ray-detected SED AGNs, six are consistent with the empirical relation of X-ray luminosity and bolometric luminosity of AGNs at $z < 3.5$, while one source has about 1 dex higher X-ray luminosity than the

empirical relation. Assuming the empirical relation, the X-ray AGNs are predicted to be Compton-thin AGNs, while the majority of X-ray-undetected SED AGNs are nearly Compton-thick AGNs. However, if we consider the X-ray weak cases, the SED AGNs can be Compton-thin AGNs.

5. In the SFR versus AGN luminosity plane, the SED AGNs are distributed in the AGN-dominant phase, while X-ray AGNs are distributed around the simultaneous evolution lines. Assuming a merger-driven evolutionary scenario, our AGN sample may correspond to the transition phase, where merging has finished but the star formation is not yet quenched. Thus, our results suggest that in such phases AGNs are likely to be heavily obscured by dust or have anomalously suppressed X-ray emissions, which makes them difficult to detect with X-ray observations.

6. The AGN number fraction in the AS2COSMOS sample is $16^{+3}_{-2}\%$ for the total (SED AGNs and X-ray AGNs) and $9\% \pm 2\%$ for only X-ray AGNs. These values are lower than the previous estimate with deeper X-ray observation, which can be attributed to the relatively shallow X-ray observations in the COSMOS field and also the selection bias of the SED AGNs.

7. Using visual classification, we identify $47^{+16}_{-15}\%$ and $25^{+6}_{-5}\%$ of the AGN hosts and galaxies without AGNs as major merger candidates, respectively. The major merger fraction in the AS2COSMOS non-AGN sample is almost consistent with the general population at $z \sim 2$. This suggests that major mergers are not necessarily required for the enhanced star formation in SMGs. On the other hand, the major merger fraction in the AS2COS-MOS AGN sample is potentially twice as high as that in the AS2COSMOS non-AGN sample. This suggests that major mergers may play a key role in triggering AGN activity in bright SMGs.

Appendix A
MIRI Images of AS2COSMOS Sources

Figure 13 shows the color-composite images of the 40 sources in the coverage of both NIRCam and MIRI. AS2COS0019.1 and AS2COS0048.1 have pointlike morphology in the MIRI/F770W band, which is consistent with the results of the SED modeling.

Figure 13. $8'' \times 8''$ JWST images of the 40 AS2COSMOS sources in the coverage of both NIRCam and MIRI imaging. The blue, green, and red colors correspond to the F115W+F150W, F277W+F444W, and F770W filters, respectively. We label the merger candidates, which have tidal features (T), disturbed morphology (D), or possible companions (C) (see Section 3.3). The major merger candidates are indicated by "M." The X-ray AGNs and SED AGNs are indicated by "X" and "SED," respectively (see Sections 3.1.3 and 4.1). Note that F150W is not used in the composite image of AS2COS0107.1 because this object is outside the coverage of F150W. For the same reason, F444W is not used in the composite image of AS2COS155.1.

Appendix B
Astrometry Check for X-Ray Sources

Figure 14(a) shows the positional offset between the X-ray source positions and the optical source positions used for the astrometry correction. After the correction, 95% of the X-ray sources have their optical counterparts within $0''.74$, which is 18% smaller than the value before the correction ($0''.90$). Then, to check the astrometric accuracy, we cross-match the X-ray source positions derived in Section 2.6.2 to the COSMOS2020 catalog. Figure 14(b) shows the histogram of the separation. For comparison, we plot the separation between the X-ray source positions in F. Civano et al. (2016) and the optical to near-infrared source positions in the COSMOS2020 catalog. We find that the median separation is about two times smaller in our catalog than in F. Civano et al. (2016). This suggests that the X-ray source positions in our catalog are better aligned with the COSMOS2020 catalog than F. Civano et al. (2016), which is likely because our

source positions are calibrated by the COSMOS2020 catalog whereas the CFHT MegaCam catalog (H. J. McCracken et al. 2012) was used as a reference in F. Civano et al. (2016).

Figure 15 shows the positions of the X-ray-detected sources near AS2COS0353.1 and AS2COS0353.2 plotted over the Ultravista K_s-band image.[21] The red points show the X-ray source positions listed in the catalog by F. Civano et al. (2016), whereas the blue points show the positions derived in our analysis. We notice a systematic offset of about $1''$ between the source positions of the two catalogs. As noticeable in panels (b) and (e) in Figure 15, the X-ray source positions in our catalog look better aligned with the Ultravista K_s-band image than those in F. Civano et al. (2016). The X-ray source in panel (c) is first identified as the X-ray counterpart of AS2COS0353.2. However, the corresponding X-ray source in our image is likely associated with AS2COS0353.1. Therefore, we consider that the X-ray source in panel (c) is associated with AS2COS0353.1.

---

[21] The K_s-band image of the COSMOS field is provided on the COSMOS website (https://cosmos.astro.caltech.edu/page/optical).
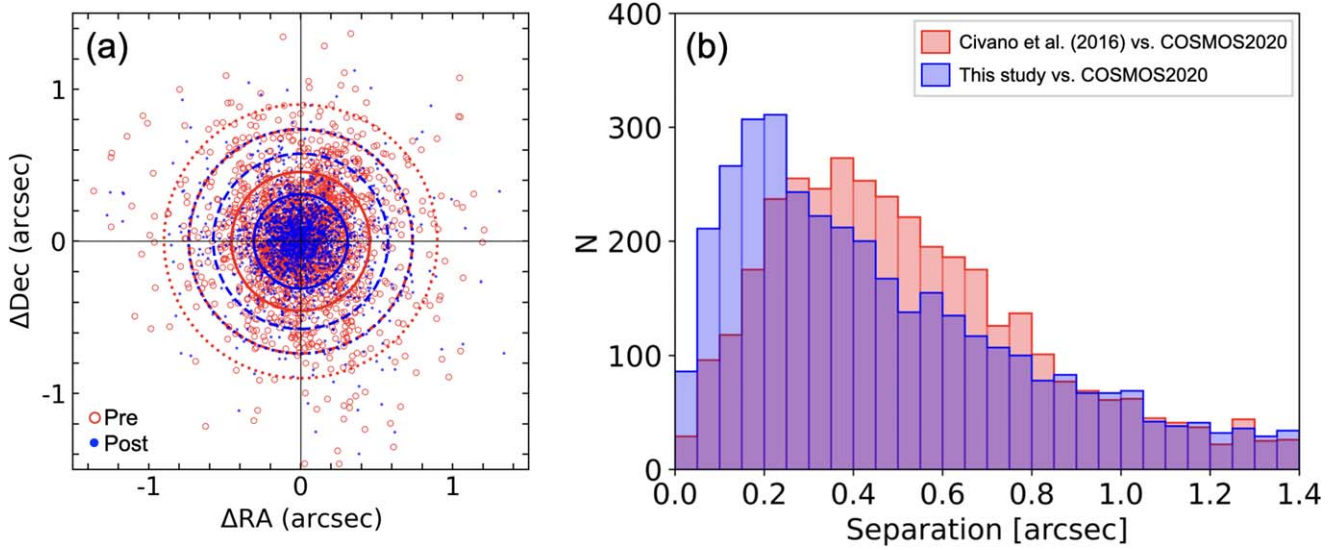
Figure 14. (a) Positional offsets between optical sources and X-ray sources used for the astrometry correction. The solid, dotted, and dashed circles encompass 68%, 90%, and 95% of the sources before (red) and after (blue) the correction, respectively. (b) Histogram of the separation between the X-ray source positions and the optical to near-infrared source positions in the COSMOS2020 catalog. The red area shows the separation between F. Civano et al. (2016) and the COSMOS2020 catalog, while the blue area denotes the separation between our X-ray source catalog (Section 2.6.2) and the COSMOS2020 catalog.
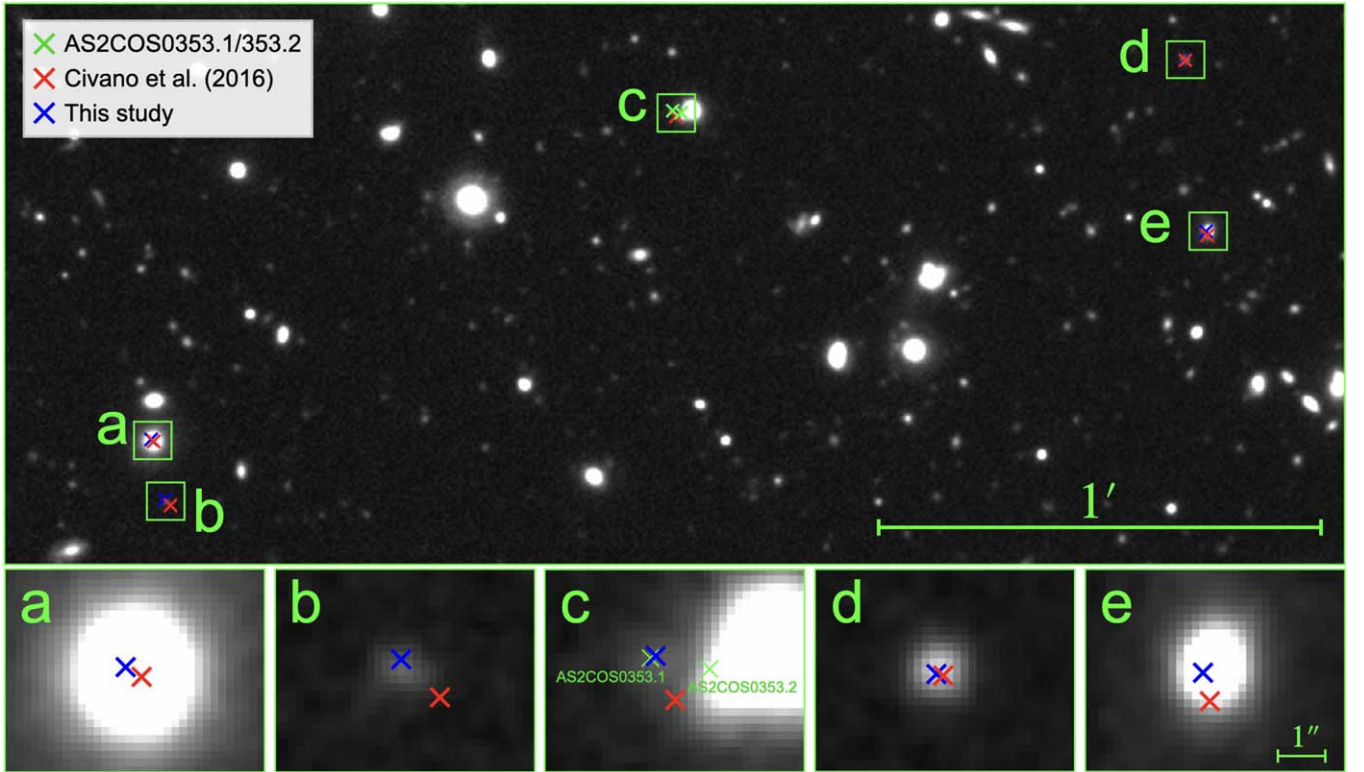
Figure 15. Positions of the X-ray-detected sources near AS2COS0353.1 and AS2COS0353.2 plotted over the Ultravista K_s-band image. The red points show the X-ray source positions listed in the catalog by F. Civano et al. (2016), whereas the blue points show the positions derived in our analysis (Section 2.6.2). The green points show the positions of AS2COS0353.1 and AS2COS0353.2. The bottom panels show the zoomed-in images of the X-ray sources.

Appendix C
Details of Iteration of the SED Modeling

In this appendix, we describe the details of the second run in SED modeling. For comparison purposes, we summarize the "basic" parameter set used in the first run in Table 2. After the first run, we notice some issues in the photometry and the parameter settings. Therefore, we add the following operations and reperform SED modeling. We confirm that these operations significantly improve the best-fit statistic.

Table 2
Basic Parameter Sets Used for the SED Modeling

Parameter	Symbol	Value
SFH (sfhdelayedbq)		
e-folding time of the main stellar population	τ_{main} (Myr)	100, 316, 1000, 3162, 10000
Age of the main stellar population	$\mathrm{age}_{\mathrm{main}}$ (Myr)	100, 158, 251, 398, 631, 1000, 1585, 2512, 3981, 6310
Age of the late burst/quench population	$\mathrm{age}_{\mathrm{bq}}$ (Myr)	10
Ratio of the SFR after/before $\mathrm{age}_{\mathrm{bq}}$	r_{SFR}	1, 10, 100, 1000
SSP (bc03; G. Bruzual & S. Charlot 2003)		
IMF of the stellar model		G. Chabrier (2003)
Metallicity of the stellar model		0.02
Dust Attenuation (dustatt_modified_starburst; D. Calzetti et al. 2000; C. Leitherer et al. 2002)		
Color excess of the nebular lines	$E(B-V)_{\mathrm{lines}}$	0.1, 0.2, 0.4, 0.6, 0.8, 1.0, 1.2, 1.4, 1.6, 1.8, 2.4, 2.8, 3.2
Reduction factor to calculate the stellar continuum attenuation	$E(B-V)_{\mathrm{factor}}$	0.44
UV bump amplitude		0 (no bump)
Power-law index to modify the attenuation curve	δ	–0.4, 0.0, 0.4
Dust Emission (EThemis; R. Uematsu et al. 2024)		
Mass fraction of the small hydrocarbon solids	q_{hac}	0.01, 0.02, 0.06, 0.10
Minimum radiation field	U_{min}	0.0, 0.4, 0.8, 1.2, 1.6, 2.0, 2.4, 3.0
Power-law index of the starlight intensity distribution	α	2.5, 3.0
Mass fraction of dust illuminated with $U = U_{\mathrm{min}}$	$1 - \gamma$	0.9
AGN Emission (skirtor2016; M. Stalevski et al. 2012, 2016)		
Average edge-on optical depth at 9.7 μm	$\tau_{9.7}$	3, 7
Radial gradient of dust density	p	1.0
Dust density gradient with polar angle	q	1.0
Half-opening angle of the dust-free cone	Δ (deg)	40
Ratio of outer to inner radius	R	20
Inclination	θ (deg)	30, 60, 80
Fraction of AGN IR luminosity to total IR luminosity	f_{AGN}	0.0, 0.1, 0.2, 0.3, 0.4, 0.5, 0.6, 0.7, 0.8, 0.9
Extinction in polar direction	$E(B-V)$	0.0, 0.1
Temperature of polar dust	T_{pol} (K)	100
Redshifting		
Redshift	z	0.1–6.0 (step size: 0.1) or fixed at spectroscopic redshifts

Note. The overall size of the parameter grid is 3,594,240,000.

C.1. Photometry Optimization

In the first run, we notice some inconsistencies between the photometry within individual sources. This can be attributed to the remaining blending effect or a failure in extracting the photometry. For these reasons, we check the images and decide to treat the following photometry as upper limits: AS2COS0001.1 (Spitzer 3.6 μm), AS2COS0043.1 (Ultravista $YJHK_s$), AS2COS0065.2 (Ultravista $YJHK_s$), and AS2COS0228.1 (Ultravista $YJHK_s$). We also treat the Ultravista $YJHK_s$ photometry of AS2COS123.1 as upper limits because we confirm no significant detection in those images. Moreover, we notice systematic offsets between the HSC $grizY$ and Ultravista $YJHK_s$ photometry of AS2COS0019.1, AS2COS0086.1, AS2COS0175.1, and AS2COS0203.1. This might be caused by calibration issues. Hence, we replace these photometry with the ones extracted from the COSMOS2020 catalog.

In addition to these operations, we optimize the photometry of some sources by referring to the HSC-SSP DR3 catalog. We replace the optical photometry of AS2COS0063.1, AS2COS0123.1, and AS2COS0228.1 with the ones extracted from the HSC-SSP DR3 catalog (H. Aihara et al. 2022). We also update the Ultravista $YJHK_s$ photometry of AS2COS0063.1 with the ones extracted from the Ultravista DR4 catalog, which appear to be less affected by a bright contaminating source. Furthermore, we exclude the Spitzer 4.5, 5.8, and 8.0 μm photometry of AS2COS0228.1 because of the significant contamination by AS2COS0228.2.

C.2. Misidentified Source

The potential optical counterpart of AS2COS0072.1 was detected in the DEIMOS 10K spectroscopic survey. They spectroscopically confirmed that the source is at $z = 0.802$ with a quality flag of $Q_f = 4$ (highest quality). However, the submillimeter line scan performed by C.-L. Liao et al. (2024) showed that AS2COS0072.1 is at $z = 3.798$. This inconsistency can be attributed to the misidentification of the counterpart. We thus regard the source at $z = 0.802$ as the foreground of AS2COS0072.1 and treat the optical to mid-infrared photometry as upper limits.

We also conclude that the optical to near-infrared counterpart of AS2COS0159.1 in HSC and Ultravista is misidentified. The high-resolution imaging by JWST revealed that there were two sources near the 870 μm source position. One was identified as a galaxy at $z = 0.033$ from the optical spectroscopy by PRIMUS. This source was initially identified as an optical counterpart of AS2COS0159.1; however, we notice that the peak wavelength of the far-infrared SED of AS2COS0159.1 is too long for a galaxy at $z = 0.033$.[22] Therefore, we consider that the source at $z = 0.033$ is foreground of AS2COS00159.1. We confirm that the foreground source was only dominant

below the F277W band. We thus decide to treat the optical to near-infrared photometry as upper limits.

C.3. SED Fitting Parameter Optimization

With the basic parameter set used in the first run, the mid- to far-infrared SED AS2COS175.1 is not well reproduced. This can be attributed to the oversimplification of the AGN component. Hence, we extend the parameter grids and recalculate the SED of these sources. The extended parameter set is summarized in Table 3.

Table 3
Extended Parameter Set of the AGN Module Used for AS2COS175.1

Parameter	Symbol	Value
AGN Emission (skirtor2016; M. Stalevski et al. 2012, 2016)		
Average edge-on optical depth at 9.7 μm	$\tau_{9.7}$	3, 5, 7, 9
Radial gradient of dust density	p	1.0
Dust density gradient with polar angle	q	1.0
Half-opening angle of the dust-free cone	Δ (deg)	40
Ratio of outer to inner radius	R	20
Inclination	θ (deg)	30, 40, 50, 60, 70, 80
Fraction of AGN IR luminosity to total IR luminosity	f_{AGN}	0.0, 0.1, 0.2, 0.3, 0.4, 0.5, 0.6, 0.7, 0.8, 0.9
Extinction in polar direction	$E(B-V)$	0.0, 0.05, 0.1
Temperature of the polar dust	T_{pol} (K)	100

---

[22] The peak of the far-infrared emission of AS2COS0159.1 is $\sim$350 μm in the observed frame. This corresponds to 9 K assuming an optically thin graybody with an emissivity index of 1.8 at $z = 0.033$.

C.4. Overall Quality of the Final Fits

Following the procedures described above, we finally obtain reasonable fits for all the sources. Figure 16 shows the histogram of the reduced χ^2 for the final fits. The median and the maximum reduced χ^2 are 1.8 and 6.5, respectively, which indicates that the SEDs are well reproduced.
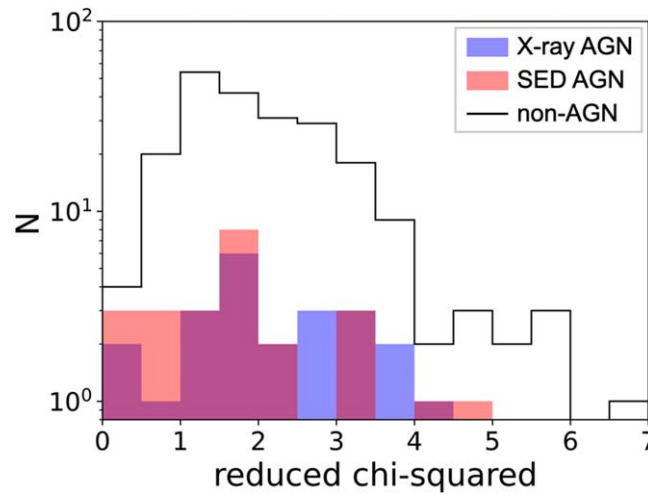
Figure 16. Histogram of the reduced χ^2 for the final fits. The median and the maximum reduced χ^2 are 1.8 and 6.5, respectively.

Appendix D
Consistency Check of SED Modeling

Figure 17 compares some observational properties with the physical properties derived by the SED modeling that they are expected to most strongly correlate with. We confirm positive correlations in these plots, supporting the validity of our SED analysis.
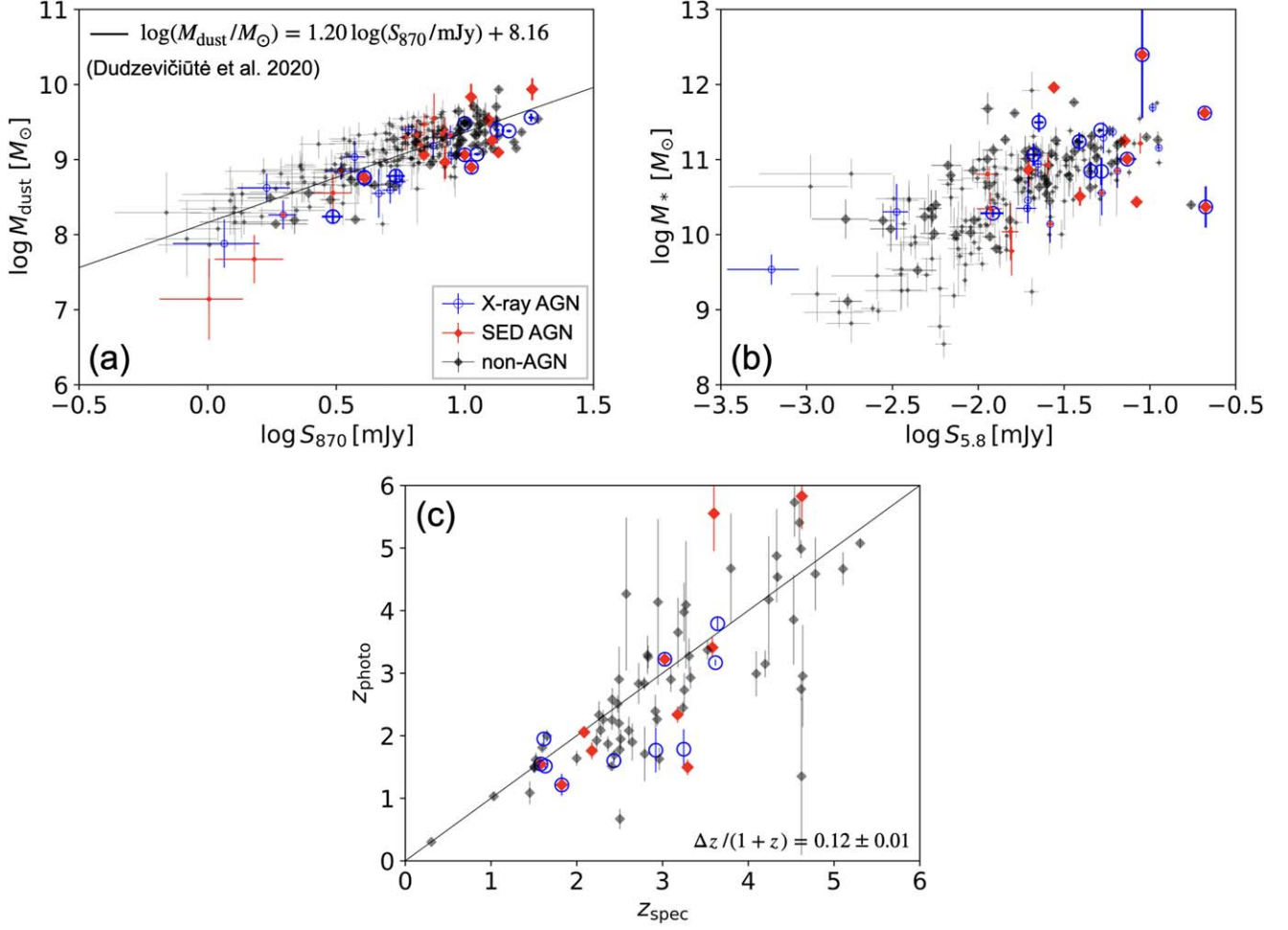
Figure 17. Comparison of the physical properties derived by the SED template fitting and the observational properties for the X-ray-detected AS2COSMOS sources (X-ray AGNs; see Section 4.1), the SED AGNs, and the rest of the AS2COSMOS sources (non-AGNs). In panels (a) and (b), the large symbols show the spec-z sample, while the smaller ones show the photo-z sample. In panel (b), the sample is limited to the sources that are detected in Spitzer 5.8 μm. In panel (c), only the spec-z sample is plotted.

Appendix E
Mock Analysis

Figure 18 compares the stellar masses and SFRs derived by CIGALE with those derived from the mock catalog. We confirm that most of the sources align well, but AS2COS0285.2 shows a large discrepancy in stellar mass, and AS2COS0175.1 shows large discrepancies in both stellar mass and SFR. AS2COS0285.2 is a galaxy without an AGN. This source is not detected in the optical band and has no spectroscopic redshift, which may make it difficult to constrain the stellar component. AS2COS0175.1 is a type 1 SED AGN. According to the SED fitting result, the optical to near-infrared SED of this source is dominated by the AGN emission, which may make the estimations unreliable. We generated pdf's of SFRs and stellar masses for several sources, including the problematic sources mentioned above. We confirmed that most of the pdf's have single-horn shapes, showing that the parameters are well constrained. However, the pdf's of AS2COS0175.1 have multihorn structures. This indicates that the SFR and stellar mass of AS2COS0175.1 are unreliable.
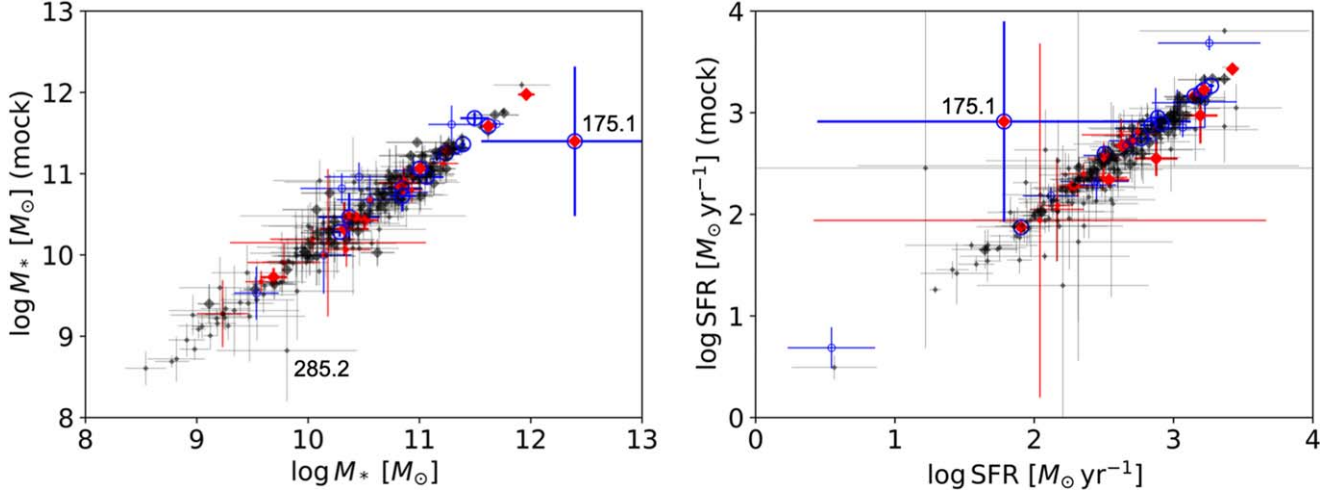
Figure 18. Comparison of the stellar mass and SFR derived by the SED analysis with those derived from the mock catalog. AS2COS0285.2 shows a large discrepancy in stellar mass, and AS2COS0175.1 shows large discrepancies in both stellar mass and SFR. The large symbols show the spec-z sample, while the smaller ones show the photo-z sample.

Appendix F
Background Modeling for Chandra ACIS-I

Table 4 summarizes the best-fit parameters of the Chandra/
ACIS-I background modeling (Section 3.2.1).

Table 4
Summary of the Background Modeling for Chandra ACIS-S (VFAINT Mode)

Model	Parameter	Value	Unit
Gaussian	E	1.487	keV
	σ	1	eV
	norm	$5.3^{+3.9}_{-3.7}$	10^{-6} photons cm^{-2} s^{-1}
Gaussian	E	1.557	keV
	σ	1	eV
	norm	$7.7^{+3.9}_{-3.7}$	10^{-6} photons cm^{-2} s^{-1}
Gaussian	E	2.123	keV
	σ	1	eV
	norm	$25.5^{+4.7}_{-4.5}$	10^{-6} photons cm^{-2} s^{-1}
Gaussian	E	2.205	keV
	σ	1	eV
	norm	$11.0^{+4.4}_{-4.2}$	10^{-6} photons cm^{-2} s^{-1}
Gaussian	E	2.410	keV
	σ	1	eV
	norm	$4.9^{+3.2}_{-3.1}$	10^{-6} photons cm^{-2} s^{-1}
Gaussian	E	2.7	keV
	σ	61^{+39}_{-45}	eV
	norm	$8.2^{+4.3}_{-3.7}$	10^{-6} photons cm^{-2} s^{-1}
Gaussian	E	7.478	keV
	σ	1	eV
	norm	$64.3^{+5.5}_{-5.3}$	10^{-6} photons cm^{-2} s^{-1}
Gaussian	E	9.713	keV
	σ	1	eV
	norm	$139.8^{+6.8}_{-6.6}$	10^{-6} photons cm^{-2} s^{-1}
Gaussian	E	9.628	keV
	σ	1	eV
	norm	linked	$1/9 \times$ norm of Au Lα_1
Gaussian	E	8.265	keV
	σ	1	eV
	norm	$14.5^{+4.2}_{-4.0}$	10^{-6} photons cm^{-2} s^{-1}
powerlaw	Γ	$0.143^{+0.026}_{-0.026}$	
	norm	$163.2^{+7.4}_{-7.4}$	10^{-6}
gabs	E	0.25	keV
	σ	153.5	eV
	Strength	$0.99^{+2.39}_{-0.66}$	10^4
expdec	α	$1.58^{+0.88}_{-0.49}$	
	norm	$3.1^{+5.6}_{-0.8}$	10^{-4}

Appendix G
Figures of Individual Sources

Figure 19 shows the X-ray spectra and best-fit models of the X-ray AGNs. Figure 20 summarizes the plots of the goodness of fit as a function of the line-of-sight hydrogen column densities. Figure 21 shows the SEDs and best-fit models of the SED AGNs.
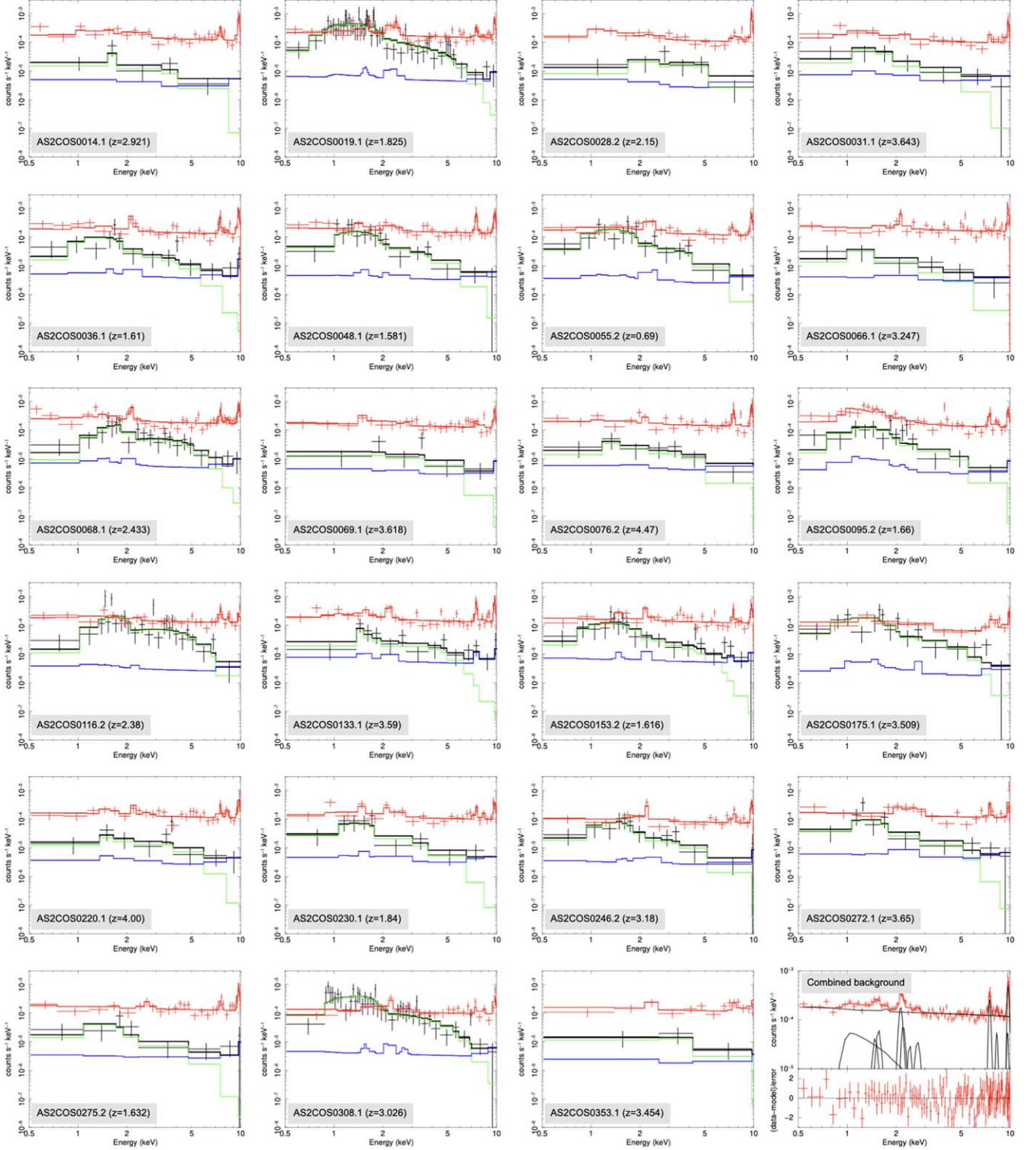
Figure 19. First 23 panels: The 0.5–10 keV spectra of the 23 X-ray AGNs (AS2COS0014.1–AS2COS0353.1). The black points and black solid lines show the observed spectra and the best-fit models, respectively. The red points and red solid lines show the background spectra and the best-fit models, respectively. The blue solid lines show the scaled background spectra. The green solid lines show the background-subtracted source spectra. To improve visibility, the source and the background spectra are binned to have at least 1.5σ and 3σ in each bin, respectively. Last panel: The combined background spectrum. The red points and red solid line show the background spectra and the best-fit model, respectively. The black solid lines show the components of the model. The lower panel shows the residuals. To improve visibility, the combined background spectrum is binned to have at least 7σ in each bin. Note that the spectrum binning only affects the presentation of the data and does not affect the spectral analysis results.
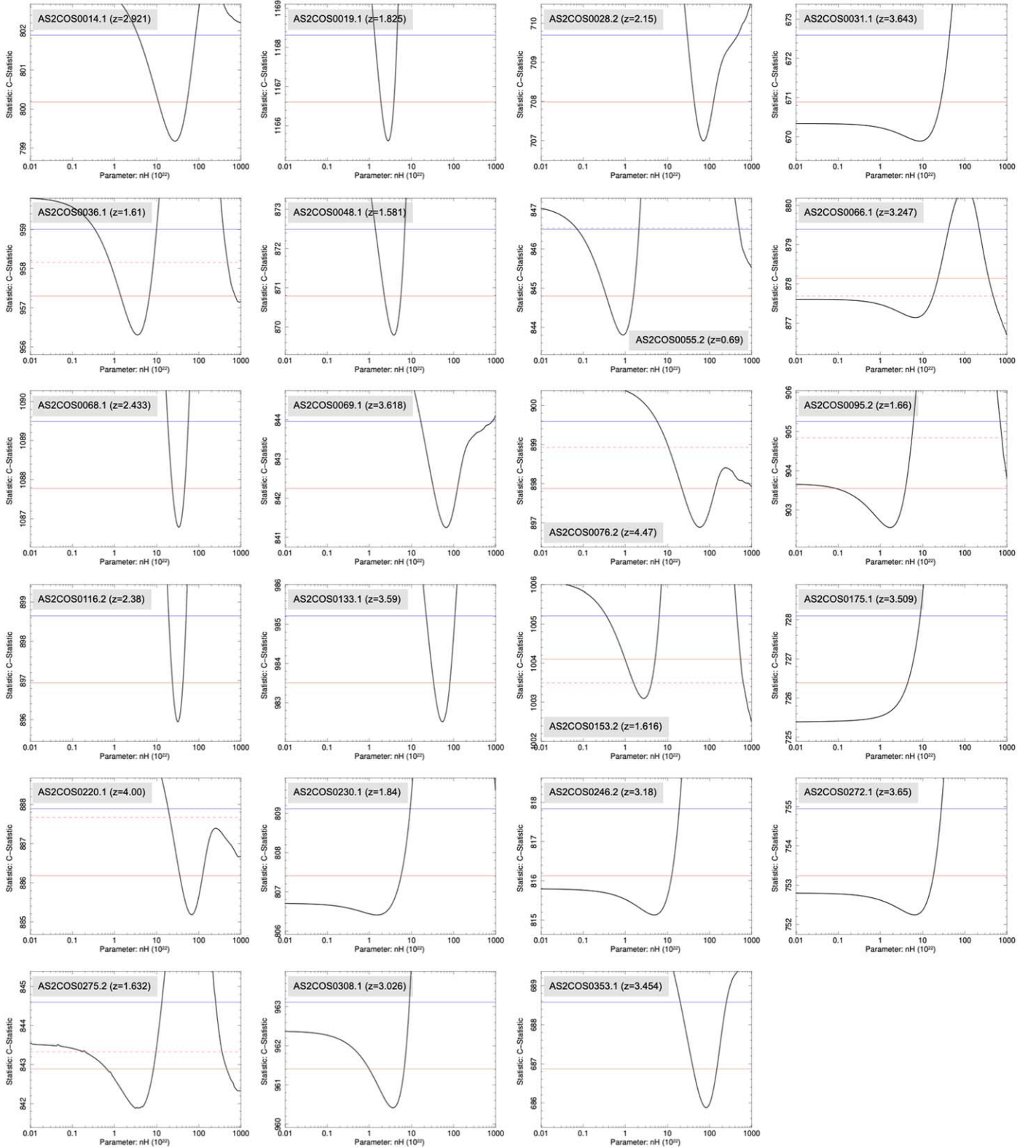
Figure 20. Plots of the goodness of fit as a function of the line-of-sight hydrogen column densities. The vertical axes show the statistical values of the *C*-statistic. The horizontal axes show the line-of-sight hydrogen column densities in units of 10^{22} cm^{-2}. The blue lines show the 90% confidence levels compared with the best-fit values. The red solid lines show the 68.27% confidence levels (1σ) compared with the Compton-thin solutions. The red dashed lines show the 68.27% confidence levels (1σ) compared with the Compton-thick solutions, if they exist.
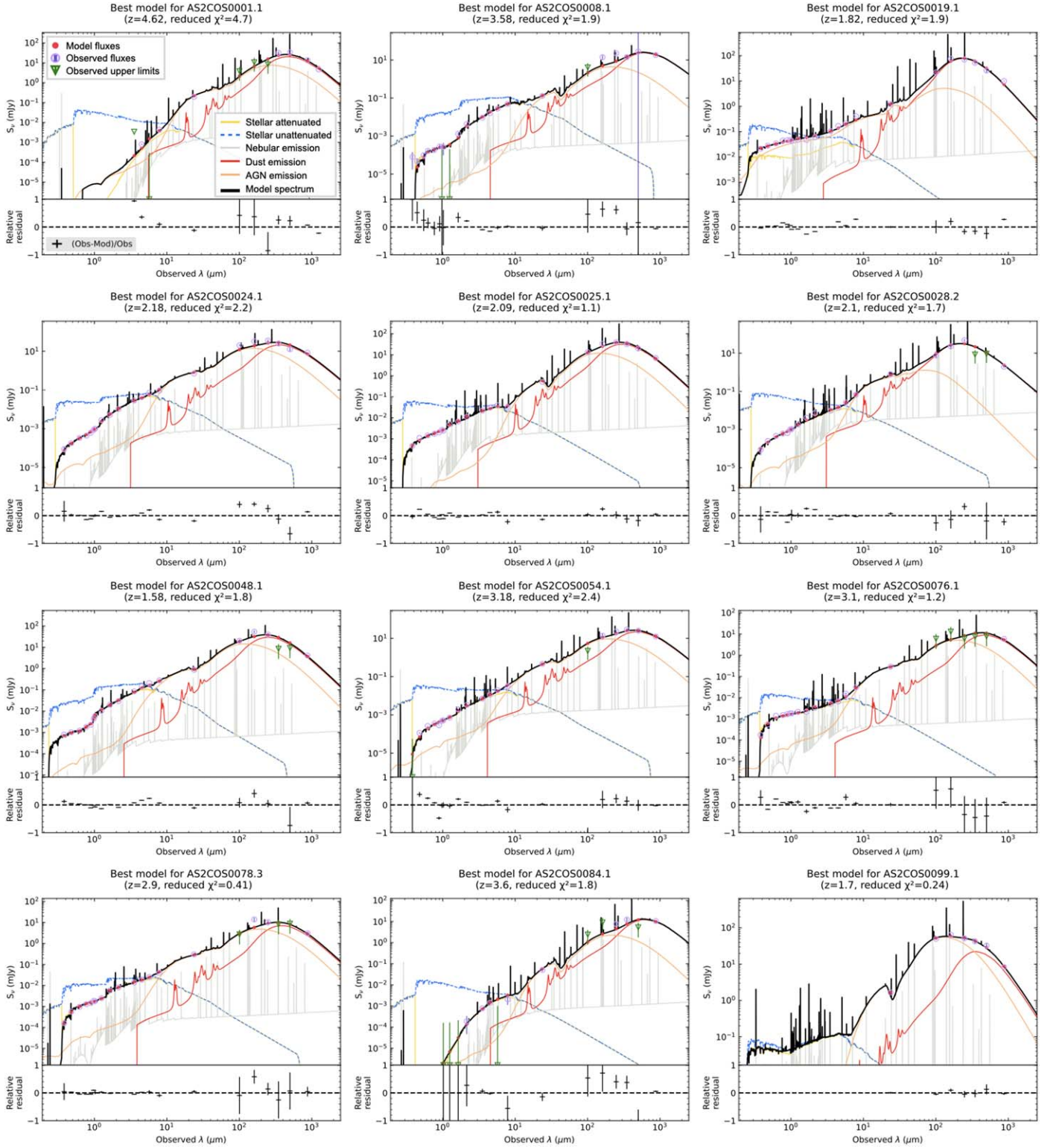
Figure 21. The SEDs and best-fit models of the SED AGNs. The black solid line represents the composite spectrum. The yellow solid line illustrates the stellar emission attenuated by interstellar dust. The blue dashed line depicts the unattenuated stellar emission for a reference purpose. The orange line corresponds to the emission from an AGN. The red line shows the infrared emission from interstellar dust. The gray line denotes the nebula emission. The observed data points are represented by purple circles, accompanied by 1σ error bars. The lower panels display the relative residuals.
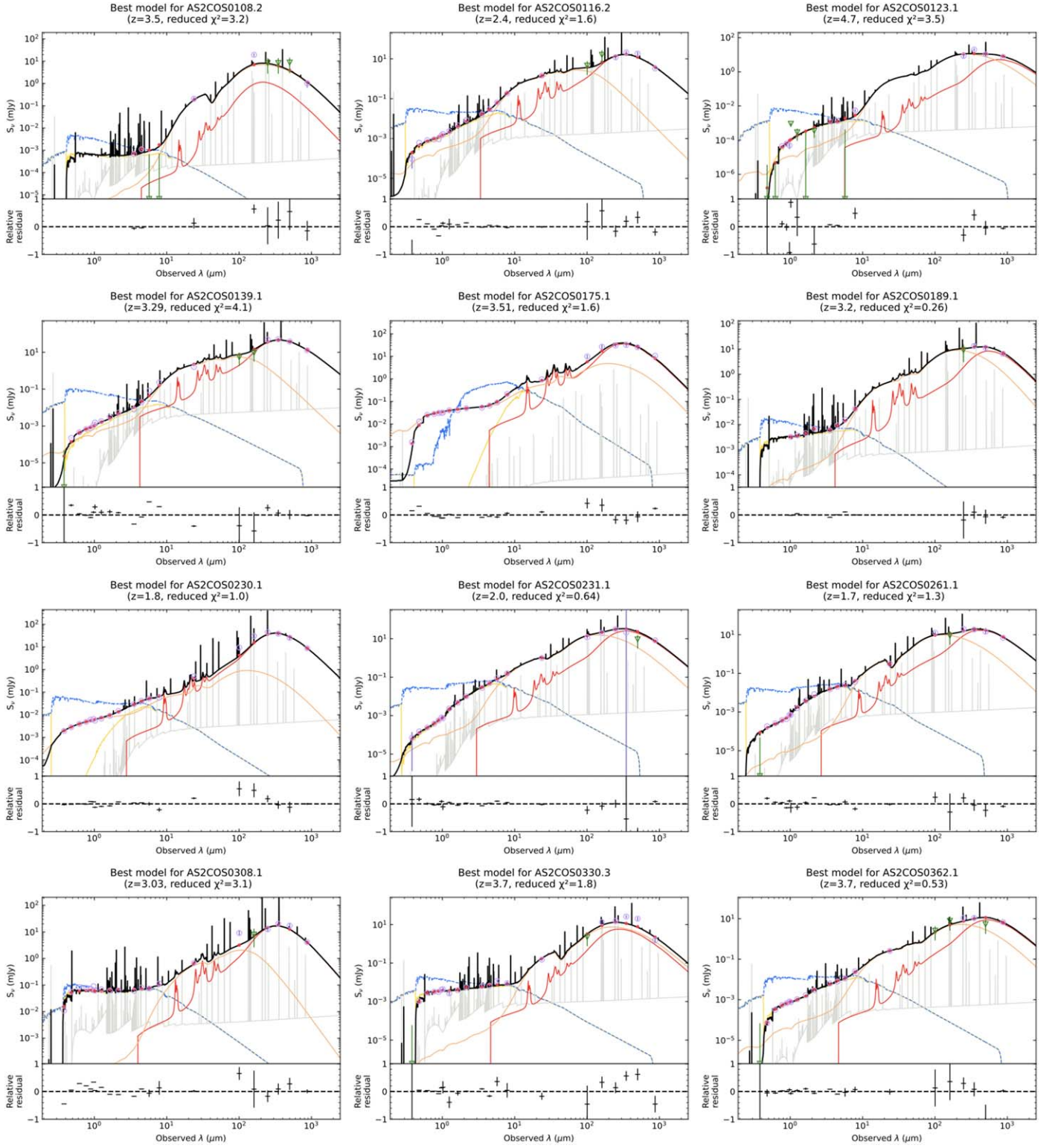
Figure 21. (Continued.)

ORCID iDs

Ryosuke Uematsu ● https://orcid.org/0000-0001-6653-779X
Yoshihiro Ueda ● https://orcid.org/0000-0001-7821-6715
David M. Alexander ● https://orcid.org/0000-0002-5896-6313
A. M. Swinbank ● https://orcid.org/0000-0003-1192-5837
Ian Smail ● https://orcid.org/0000-0003-3037-257X
Carolina Andonie ● https://orcid.org/0000-0002-5580-4298
Chian-Chou Chen ● https://orcid.org/0000-0002-3805-0789
Ugne Dudzevičiūtė ● https://orcid.org/0000-0003-4748-0681
Kotaro Kohno ● https://orcid.org/0000-0002-4052-2394
Yuichi Matsuda ● https://orcid.org/0000-0003-1747-2891
Annagrazia Puglisi ● https://orcid.org/0000-0001-9369-1805
Hideki Umehata ● https://orcid.org/0000-0003-1937-0573
Wei-Hao Wang ● https://orcid.org/0000-0003-2588-1265

References

Ahumada, R., Allende Prieto, C., Almeida, A., et al. 2020, ApJS, 249, 3
Aihara, H., AlSayyad, Y., Ando, M., et al. 2019, PASJ, 71, 114
Aihara, H., AlSayyad, Y., Ando, M., et al. 2022, PASJ, 74, 247
Alexander, D. M., Bauer, F. E., Chapman, S. C., et al. 2005, ApJ, 632, 736
Alexander, D. M., & Hickox, R. C. 2012, NewAR, 56, 93
Algera, H. S. B., Smail, I., Dudzevičiūtė, U., et al. 2020, ApJ, 903, 138
Andonie, C., Alexander, D. M., Greenwell, C., et al. 2024, MNRAS, 527, L144
Andonie, C., Alexander, D. M., Rosario, D., et al. 2022, MNRAS, 517, 2577
Arnaud, K. A. 1996, in ASP Conf. Ser. 101, Astronomical Data Analysis Software and Systems V, ed. G. H. Jacoby & J. Barnes (San Francisco, CA: ASP), 17
Astropy Collaboration, Price-Whelan, A. M., Sipőcz, B. M., et al. 2018, AJ, 156, 123
Astropy Collaboration, Robitaille, T. P., Tollerud, E. J., et al. 2013, A&A, 558, A33
Barger, A. J., Cowie, L. L., Bauer, F. E., & González-López, J. 2019, ApJ, 887, 23
Barger, A. J., Cowie, L. L., Blair, A. H., & Jones, L. H. 2022, ApJ, 934, 56
Birkin, J. E., Weiss, A., Wardlow, J. L., et al. 2021, MNRAS, 501, 3926
Boquien, M., Burgarella, D., Roehlly, et al. 2019, A&A, 622, A103
Bower, R. G., Benson, A. J., Malbon, R., et al. 2006, MNRAS, 370, 645
Bruzual, G., & Charlot, S. 2003, MNRAS, 344, 1000
Calzetti, D., Armus, L., Bohlin, R. C., et al. 2000, ApJ, 533, 682
Casey, C. M., Kartaltepe, J. S., Drakos, N. E., et al. 2023, ApJ, 954, 31
Cash, W. 1979, ApJ, 228, 939
Chabrier, G. 2003, PASP, 115, 763
Chapman, S. C., Blain, A. W., Smail, I., & Ivison, R. J. 2005, ApJ, 622, 772
Chen, C.-C., Liao, C.-L., Smail, I., et al. 2022, ApJ, 929, 159
Chien, T. C. C., Ling, C.-T., Goto, T., et al. 2024, MNRAS, 532, 719
Civano, F., Marchesi, S., Comastri, A., et al. 2016, ApJ, 819, 62
Coil, A. L., Blanton, M. R., Burles, S. M., et al. 2011, ApJ, 741, 8
Condon, J. J. 1992, ARA&A, 30, 575
Cool, R. J., Moustakas, J., Blanton, M. R., et al. 2013, ApJ, 767, 118
Cowie, L. L., Barger, A. J., Hsu, L. Y., et al. 2017, ApJ, 837, 139
Cowie, L. L., González-López, J., Barger, A. J., et al. 2018, ApJ, 865, 106
Damjanov, I., Zahid, H. J., Geller, M. J., Fabricant, D. G., & Hwang, H. S. 2018, ApJS, 234, 21
Delvecchio, I., Daddi, E., Sargent, M. T., et al. 2021, A&A, 647, A123
Donley, J. L., Koekemoer, A. M., Brusa, M., et al. 2012, ApJ, 748, 142
Dudzevičiūtė, U., Smail, I., Swinbank, A. M., et al. 2020, MNRAS, 494, 3828
Dunlop, J. S., Abraham, R. G., Ashby, M. L. N., et al. 2021, PRIMER: Public Release IMaging for Extragalactic Research JWST Proposal. Cycle 1, ID. #1837
Duras, F., Bongiorno, A., Ricci, F., et al. 2020, A&A, 636, A73
Elvis, M., Civano, F., Vignali, C., et al. 2009, ApJS, 184, 158
Elvis, M., Wilkes, B. J., McDowell, J. C., et al. 1994, ApJS, 95, 1
Fabian, A. C. 2012, ARA&A, 50, 455
Fruscione, A., McDowell, J. C., Allen, G. E., et al. 2006, Proc. SPIE, 6270, 62701V
Fu, J., Kauffmann, G., Li, C., & Guo, Q. 2012, MNRAS, 424, 2701
Fujimoto, S., Ouchi, M., Kohno, K., et al. 2018, ApJ, 861, 7
Gao, F., Wang, L., Pearson, W. J., et al. 2020, A&A, 637, A94
Gillman, S., Smail, I., Gullberg, B., et al. 2024, A&A, 691, A299
Goulding, A. D., Greene, J. E., Bezanson, R., et al. 2018, PASJ, 70, S37

Gullberg, B., Smail, I., Swinbank, A. M., et al. 2019, MNRAS, 490, 4956
Hasinger, G., Capak, P., Salvato, M., et al. 2018, ApJ, 858, 77
Hatsukade, B., Kohno, K., Yamaguchi, Y., et al. 2018, PASJ, 70, 105
Hayward, C. C., Narayanan, D., Kereš, D., et al. 2013, MNRAS, 428, 2529
Hickox, R. C., & Alexander, D. M. 2018, ARA&A, 56, 625
Hobbs, A., Nayakshin, S., Power, C., & King, A. 2011, MNRAS, 413, 2633
Hodge, J. A., Karim, A., Smail, I., et al. 2013, ApJ, 768, 91
Hodge, J. A., Smail, I., Walter, F., et al. 2019, ApJ, 876, 130
Hodge, J. A., Swinbank, A. M., Simpson, J. M., et al. 2016, ApJ, 833, 103
Hopkins, P. F., Hernquist, L., Cox, T. J., & Kereš, D. 2008, ApJS, 175, 356
Hsieh, B.-C., Wang, W.-H., Hsieh, C.-C., et al. 2012, ApJS, 203, 23
Hwang, Y.-H., Wang, W.-H., Chang, Y.-Y., et al. 2021, ApJ, 913, 6
Ibar, E., Ivison, R. J., Best, P. N., et al. 2010, MNRAS, 401, L53
Ibar, E., Ivison, R. J., Biggs, A. D., et al. 2009, MNRAS, 397, 281
Ikarashi, S., Caputi, K. I., Ohta, K., et al. 2017, ApJL, 849, L36
Ikarashi, S., Ivison, R. J., Caputi, K. I., et al. 2015, ApJ, 810, 133
Iono, D., Peck, A. B., Pope, A., et al. 2006, ApJL, 640, L1
Jin, S., Daddi, E., Liu, D., et al. 2018, ApJ, 864, 56
Jin, S., Sillassen, N. B., Hodge, J., et al. 2024, A&A, 690, L16
Jones, A. P., Köhler, M., Ysard, N., Bocchio, M., & Verstraete, L. 2017, A&A, 602, A46
Kalberla, P. M. W., Burton, W. B., Hartmann, D., et al. 2005, A&A, 440, 775
Kashino, D., Silverman, J. D., Sanders, D., et al. 2019, ApJS, 241, 10
Kashyap, V. L., van Dyk, D. A., Connors, A., et al. 2010, ApJ, 719, 900
Kennicutt, R. C. J. 1998, ApJ, 498, 541
Kocevski, D. D., Faber, S. M., Mozena, M., et al. 2012, ApJ, 744, 148
Kocevski, D. D., Hasinger, G., Brightman, M., et al. 2018, ApJS, 236, 48
Komatsu, E., Smith, K. M., Dunkley, J., et al. 2011, ApJS, 192, 18
Kormendy, J., & Ho, L. C. 2013, ARA&A, 51, 511
Lagos, C. D. P., Baugh, C. M., Lacey, C. G., et al. 2011, MNRAS, 418, 1649
Laigle, C., McCracken, H. J., Ilbert, O., et al. 2016, ApJS, 224, 24
Laloux, B., Georgakakis, A., Andonie, C., et al. 2023, MNRAS, 518, 2546
Le Fèvre, O., Cassata, P., Cucciati, O., et al. 2013, A&A, 559, A14
Leitherer, C., Li, I. H., Calzetti, D., & Heckman, T. M. 2002, ApJS, 140, 303
Liao, C.-L., Chen, C.-C., Wang, W.-H., et al. 2024, ApJ, 961, 226
Lilly, S. J., Le Brun, V., Maier, C., et al. 2009, ApJS, 184, 218
Lutz, D., Poglitsch, A., Altieri, B., et al. 2011, A&A, 532, A90
Madau, P., & Dickinson, M. 2014, ARA&A, 52, 415
Magnelli, B., Lutz, D., Santini, P., et al. 2012, A&A, 539, A155
Marian, V., Jahnke, K., Mechtley, M., et al. 2019, ApJ, 882, 141
Masters, D. C., Stern, D. K., Cohen, J. G., et al. 2019, ApJ, 877, 81
McAlpine, S., Smail, I., Bower, R. G., et al. 2019, MNRAS, 488, 2440
McCracken, H. J., Milvang-Jensen, B., Dunlop, J., et al. 2012, A&A, 544, A156
McKinney, J., Casey, C. M., Long, A. S., et al. 2024, arXiv:2408.08346
Mechtley, M., Jahnke, K., Windhorst, R. A., et al. 2016, ApJ, 830, 156
Mitsuhashi, I., Matsuda, Y., Smail, I., et al. 2021, ApJ, 907, 122
Miyaji, T., Griffiths, R. E. & C-COSMOS Team 2008, AAS HEAD Meeting, 10, 4.01
Momcheva, I. G., Brammer, G. B., van Dokkum, P. G., et al. 2016, ApJS, 225, 27
Nandra, K., Barret, D., Barcons, X., et al. 2013, arXiv:1306.2307
Noll, S., Burgarella, D., Giovannoli, E., et al. 2009, A&A, 507, 1793
Ogawa, S., Ueda, Y., Tanimoto, A., & Yamada, S. 2021, ApJ, 906, 84
Ogawa, S., Ueda, Y., Yamada, S., Tanimoto, A., & Kawaguchi, T. 2019, ApJ, 875, 115
Oke, J. B., & Gunn, J. E. 1983, ApJ, 266, 713
Oliver, S. J., Bock, J., Altieri, B., et al. 2012, MNRAS, 424, 1614
Pearson, J., Serjeant, S., Wang, W.-H., et al. 2024, MNRAS, 527, 12044
Pope, A., Chary, R.-R., Alexander, D. M., et al. 2008, ApJ, 675, 1171
Ricci, C., Privon, G. C., Pfeifle, R. W., et al. 2021, MNRAS, 506, 5935
Sanders, D. B., Salvato, M., Aussel, H., et al. 2007, ApJS, 172, 86
Sazonov, S., & Khabibullin, I. 2017, MNRAS, 468, 2249
Schartmann, M., Meisenheimer, K., Camenzind, M., Wolf, S., & Henning, T. 2005, A&A, 437, 861
Silverman, J. D., Kashino, D., Sanders, D., et al. 2015, ApJS, 220, 12
Simpson, J. M., Smail, I., Dudzevičiūtė, U., et al. 2020, MNRAS, 495, 3409
Simpson, J. M., Smail, I., Swinbank, A. M., et al. 2015, ApJ, 799, 81
Simpson, J. M., Smail, I., Swinbank, A. M., et al. 2017, ApJ, 839, 58
Simpson, J. M., Smail, I., Swinbank, A. M., et al. 2019, ApJ, 880, 43
Skelton, R. E., Whitaker, K. E., Momcheva, I. G., et al. 2014, ApJS, 214, 24
Smolčić, V., Novak, M., Bondi, M., et al. 2017, A&A, 602, A1
Stach, S. M., Dudzevičiūtė, U., Smail, I., et al. 2019, MNRAS, 487, 4648
Stach, S. M., Smail, I., Swinbank, A. M., et al. 2018, ApJ, 860, 161
Stalevski, M., Fritz, J., Baes, M., Nakos, T., & Popović, L. Č. 2012, MNRAS, 420, 2756

Stalevski, M., Ricci, C., Ueda, Y., et al. 2016, MNRAS, 458, 2288
Steinhardt, C. L., Speagle, J. S., Capak, P., et al. 2014, ApJL, 791, L25
Suzuki, H., Plucinsky, P. P., Gaetz, T. J., & Bamba, A. 2021, A&A, 655, A116
Swinbank, A. M., Simpson, J. M., Smail, I., et al. 2014, MNRAS, 438, 1267
Tamura, Y., Iono, D., Wilner, D. J., et al. 2010, ApJ, 724, 1270
Tanimoto, A., Ueda, Y., Odaka, H., et al. 2019, ApJ, 877, 95
Teng, S. H., Brandt, W. N., Harrison, F. A., et al. 2014, ApJ, 785, 19
Toba, Y., Goto, T., Oi, N., et al. 2020, ApJ, 899, 35
Torres-Albà, N., Iwasawa, K., Dìaz-Santos, T., et al. 2018, A&A, 620, A140
Ueda, Y., Akiyama, M., Hasinger, G., Miyaji, T., & Watson, M. G. 2014, ApJ, 786, 104
Ueda, Y., Akiyama, M., Ohta, K., & Miyaji, T. 2003, ApJ, 598, 886
Ueda, Y., Hatsukade, B., Kohno, K., et al. 2018, ApJ, 853, 24
Uematsu, R., Ueda, Y., Kohno, K., et al. 2024, ApJ, 965, 108

Umehata, H., Fumagalli, M., Smail, I., et al. 2019, Sci, 366, 97
Umehata, H., Tamura, Y., Kohno, K., et al. 2015, ApJL, 815, L8
Villforth, C. 2023, OJAp, 6, 34
Wang, S. X., Brandt, W. N., Luo, B., et al. 2013, ApJ, 778, 179
Wang, T., Elbaz, D., Daddi, E., et al. 2016, ApJ, 828, 56
Weaver, J. R., Kauffmann, O. B., Ilbert, O., et al. 2022, ApJS, 258, 11
Weisskopf, M. C., Brinkman, B., Canizares, C., et al. 2002, PASP, 114, 1
Willingale, R., Starling, R. L. C., Beardmore, A. P., Tanvir, N. R., & O'Brien, P. T. 2013, MNRAS, 431, 394
Yamada, S., Ueda, Y., Tanimoto, A., et al. 2021, ApJS, 257, 61
Yang, G., Boquien, M., Brandt, W. N., et al. 2022, ApJ, 927, 192
Yang, G., Boquien, M., Buat, V., et al. 2020, MNRAS, 491, 740
Yang, G., Caputi, K. I., Papovich, C., et al. 2023, ApJL, 950, L5
Younger, J. D., Fazio, G. G., Wilner, D. J., et al. 2008, ApJ, 688, 59